



Mathematical Modeling of Tumor Immune Interactions: The Role of Anti-FGFR and Anti-PD-1 in the Combination Therapy

Chenghang Li¹ · Zonghang Ren¹ · Guiyu Yang² · Jinzhi Lei^{1,3}

Received: 12 March 2024 / Accepted: 13 June 2024

© The Author(s), under exclusive licence to the Society for Mathematical Biology 2024

Abstract

Bladder cancer poses a significant global health burden with high incidence and recurrence rates. This study addresses the therapeutic challenges in advanced bladder cancer, focusing on the competitive mechanisms of ligand or drug binding to receptors. We developed a refined mathematical model that integrates the dynamics of tumor cells and immune responses, particularly targeting fibroblast growth factor receptor 3 (FGFR3) and immune checkpoint inhibitors (ICIs). This study contributes to understanding combination therapies by elucidating the competitive binding dynamics and quantifying the synergistic effects. The findings highlight the importance of personalized immunotherapeutic strategies, considering factors such as drug dosage, dosing schedules, and patient-specific parameters. Our model further reveals that ligand-independent activated-state receptors are the most essential drivers of tumor proliferation. Moreover, we found that PD-L1 expression rate was more important than PD-1 in driving the dynamic evolution of tumor and immune cells. The proposed mathematical model provides a comprehensive framework for unraveling the complexities of combination therapies in advanced bladder cancer. As research progresses, this multidisciplinary approach contributes valuable insights toward optimizing therapeutic strategies and advancing cancer treatment paradigms.

Keywords Bladder cancer · Tumor microenvironment · Targeted therapy · Immunotherapy · Combination therapy · Mathematical model

✉ Jinzhi Lei
jzlei@tiangong.edu.cn

¹ School of Mathematical Sciences, Tiangong University, Tianjin 300387, China

² School of Computer Science and Technology, Tiangong University, Tianjin 300387, China

³ Center for Applied Mathematics, Tiangong University, Tianjin 300387, China

1 Introduction

Bladder cancer ranks among the most common malignant tumors of the urinary system, marked by a comparatively high incidence and recurrence rate (Patel et al. 2020; Lenis et al. 2020). From a genetic perspective, the prevailing belief is that cancer cells arise from somatic mutations resulting from a combination of DNA damage and repair processes (Alexandrov et al. 2013). Recent years have witnessed intensive research on the pathogenesis of bladder cancer, leading to the further optimization of therapeutic strategies tailored to different stages and types of the disease (Robertson et al. 2017; Cancer Genome Atlas Research 2014). Bacillus Calmette-Guerin (BCG) is the primary therapeutic regimen for early-stage non-muscle invasive bladder cancer (Singh et al. 2022; Biot et al. 2012). Conversely, in advanced muscle-invasive bladder cancer, while targeted therapy or immunotherapy may benefit certain patients, the majority experience tumor recurrence (Benjamin and Hsu 2023; Morales-Barrera et al. 2016; Patel et al. 2020; Lenis et al. 2020). Prolonging overall patient survival and addressing tumor recurrence constitute pivotal challenges in current scientific research. Clinical outcomes underscore the efficacy of combination therapy in significantly delaying tumor recurrence, enhancing both the progression-free and overall survival for patients (Tran et al. 2021; Patel et al. 2020). However, a notable gap persists in the absence of a mathematical model elucidating combination therapy from the competitive mechanisms of ligand or drug binding to the receptor.

Targeted therapy directed at the fibroblast growth factor receptor (FGFR) on the surface of tumor cells is a key therapeutic approach for advanced bladder cancer (Katoh 2019). The binding of fibroblast growth factor (FGF) to FGFR triggers the phosphorylation of the intracellular kinase structural domain of FGFR. This process activates downstream signaling pathways, including RAS-RAF-MAPK, PI3K-AKT, STAT, and PLC γ , crucial in regulating cell proliferation and survival (Katoh 2019; Lemmon and Schlessinger 2010). Given that the overexpression or mutation of FGFR3 is a common characteristic of bladder cancer, FGFR3 has emerged as an effective therapeutic target for treating this malignancy (Katoh 2019; Lemmon and Schlessinger 2010; Rozen 2020; Babina and Turner 2017). Despite the demonstrated effectiveness of targeted therapy in treating bladder cancer, its benefits remain confined, primarily influenced by the level of activated-state FGFR expression on the surface of tumor cells (Maeng et al. 2010; Tomlinson et al. 2007).

Bladder cancer has been at the forefront of early immunotherapy trials, showcasing a notably remarkable immunotherapeutic effect compared to various tumor types (Ward Grados et al. 2022; Khalife et al. 2021). In the past decade, immune checkpoint inhibitors (ICIs) have gained widespread use in the clinical treatment of patients with melanoma and non-small cell lung cancer (Hamid et al. 2013; Schachter et al. 2017; Rizvi et al. 2015). It is noteworthy that only in recent years have ICIs been extensively employed in the clinical treatment of bladder cancer, demonstrating excellent treatment efficacy (Emens et al. 2017; Wołaciewicz et al. 2020). The expression of PD-L1 on tumor cells provides an effective mechanism for tumor immune escape, interacting with PD-1 on the surface of T cells to inhibit T cell proliferation, differentiation, and the killing function (Tumeh et al. 2014). ICIs play a crucial role in blocking the formation of PD-1-PD-L1 complexes, thereby restoring immune cell function and impeding

the progression of tumor cells (Yamaguchi et al. 2022). Clinical trials have consistently shown the favorable efficacy of ICIs in treating bladder cancer, heralding a new therapeutic paradigm for patients with high PD-L1 expression on tumor cell surface (Powles et al. 2014; Apolo et al. 2017). ICIs can usually induce durable responses, notwithstanding their correspondingly lower response efficiency (Sharma and Allison 2015). However, the utilization of ICIs is influenced by drug dosage and treatment schedules, as patients often grapple with severe systemic side effects and the risk of tumor recurrence.

Targeted therapy at the FGFR3 mutation site can suppress cancer cell proliferation and typically exhibits high response efficiency, albeit with a brief response duration. However, FGFR inhibitors can increase PD-L1 expression in the tumor cell and lead to an immunosuppressive effect on T cells (Jing et al. 2022). Combining ICIs with FGFR inhibitors can prevent the immunosuppressive effect and restore T cell function, achieving a synergistic effect between targeted therapy and immunotherapy. The utilization of FGFR inhibitors in combination therapy with ICIs for bladder cancer is substantiated and has demonstrated positive therapeutic efficacy in clinical treatment (Sharma and Allison 2015).

Mathematical models have been extensively applied to understand the dynamics of tumor immune interactions. In the 1990s, Kuznetsov et al. (1994) applied the Lotka-Volterra model to describe the dynamics of immune interactions in tumors. Subsequently, Kirschner and Panetta (1998) further established a mathematical model for the dynamic regulatory network between interleukin-2, tumor cells, and effector cells. de Pillis et al. (2005) carved out the role of innate (NK cells) and adaptive (CD8⁺T cells) immune cells in tumor immune surveillance. Meanwhile, Robertson-Tessi et al. (2012) proposed a systematic mathematical model of tumor-immune interactions, which suggests a negative feedback loop to the activation of the immune system by introducing immunosuppressive mechanisms. On this basis, Soto-Ortiz and Finley (2016) developed a mathematical model that couples antiangiogenic therapy targeting the tumor vascular system and immunotherapy targeting the tumor. In recent years, mathematical models based on therapies such as chemotherapy, cancer vaccines, cytokine inhibitors, and immune checkpoint inhibitors have gradually been developed (Lai and Friedman 2017b; Nikolopoulou et al. 2018; Yu and Jang 2019; Siewe and Friedman 2021; Kozłowska et al. 2020; Liao and Watt 2022; Ma et al. 2023; Xue et al. 2023), further expanding the application of mathematical models in tumor therapy.

Additionally, various mathematical models were developed to reveal the dynamic evolution and treatment effects of bladder cancer (Shaikh and Bunimovich-Mendrazitsky 2018; Lazebnik et al. 2021; Breban et al. 2012; Burgos-Simón et al. 2019; Okuneye et al. 2021). Shaikh and Bunimovich-Mendrazitsky (2018) established a mathematical model for BCG treatment of bladder cancer through ordinary differential equations. Meanwhile, Lazebnik et al. (2021) developed a mathematical model for BCG treatment of bladder cancer. This model describes the geometric distribution of cancer cells in the bladder using partial differential equations, thus providing a quantitative description of the depth of the tumor polyps. Breban et al. (2012) further tested the limitations of the innate immune response during BCG treatment of non-muscle invasive bladder cancer. Burgos-Simón et al. (2019) proposed a mathe-

mathematical model describing the dynamic evolution of bladder tumor growth and immune response.

In a study by Okuneye et al. (2021), a mathematical model was developed for muscle-invasive bladder cancer based on the biological understanding of the bladder cancer growth in the presence of the FGFR3. The model describes the impact of ligand-independent activation of FGFR3 on tumor growth and cytotoxic T cell (CTL) mediated death before treatment. It was then extended to include anti-PD-L1 therapy, evaluating the combined use of an FGFR3 inhibitor and anti-PD-1/PD-L1 monoclonal antibody. The findings suggest that anti-PD-L1 therapy is less effective in the presence of FGFR3 mutations, highlight the conditions where monotherapies perform well, and emphasize the superiority of anti-PD-L1 pretreatment in achieving greater tumor reduction. These studies contribute to the development of personalized immunotherapeutic strategies tailored to individual patient profiles. However, further refinement and validation of mathematical models incorporating the evolving landscape of immunotherapeutic agents are needed to enhance their predictive accuracy and clinical relevance.

The objective of the current study was to create an advanced mathematical model of the tumor immune microenvironment. This model aimed to characterize tumor proliferation based on the activated state of FGFR receptors on the surface of tumor cells while incorporating targeted drugs' impact on tumor growth. Additionally, a target competition model is being developed to consider the influence of ICIs by examining the competitive binding of PD-1 to PD-L1 and anti-PD-L1, and by analyzing the specific expression of the PD-1-PD-L1 complex. The study also includes an analysis of drug dosage and dosing schedule to better understand the therapeutic effects and potential strategies for combination therapy.

2 Mathematical Model

2.1 Multiscale Mathematical Model of Tumor Microenvironment

Figure 1 illustrates the dynamic regulation network of the tumor microenvironment within bladder cancer tissues, highlighting the combined action of various immune cells and cytokines (Schneider et al. 2019; Lai et al. 2018; Chen and Mellman 2013). Within the tumor microenvironment, dendritic cells, as initiators of the body's immune response, capture and process antigens released by tumor cells through MHC molecules on their surface (Jensen 2007; Gardner and Ruffell 2016). Subsequently, these dendritic cells present tumor-specific antigens to naive CD4⁺T cells. In response to cytokine interactions in the surrounding environment, naive CD4⁺T cells further differentiate into different types of effector T cells, including helper T cells and regulatory T cells (Zhu and Paul 2008; Zhou et al. 2009; Dong 2021). Meanwhile, naive CD8⁺T cells differentiate into cytotoxic T lymphocytes after antigenic stimulation, playing a crucial role in the anti-tumor immune response (Tscharke et al. 2015). Throughout the dynamic process of the tumor microenvironment, macrophages exhibit two distinct phenotypes, M1 and M2, exerting anti-tumor and pro-tumor effects, respectively

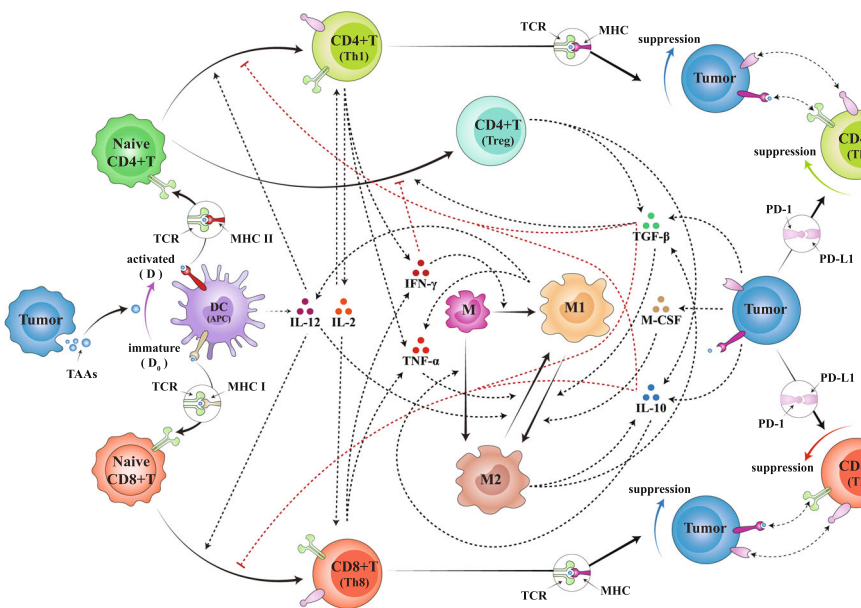


Fig. 1 Dynamic regulatory networks in the tumor microenvironment within bladder cancer tissues. Immature dendritic cells capture antigens released by tumor cells through MHC molecules on their surface, transforming them into an activated state and exerting antigen-presenting functions. To recognize tumor-specific antigens, naive CD4⁺T cells and naive CD8⁺T cells connect to MHCII and MHC I through the T cell antigen receptor (TCR), respectively. Naive CD4⁺T cells differentiate into Th1 cells in response to IL-12, a process inhibited by IL-10 and TGF- β . Th1 cells proliferate in response to their secretion of IL-2. Additionally, naive CD4⁺T cells can differentiate into Treg cells in response to TGF- β , a process inhibited by IFN- γ . Naive CD8⁺T cells differentiate into CTL cells in response to IL-12, a process inhibited by IL-10 and TGF- β . Furthermore, CTL cells can proliferate in response to IL-2 secreted by Th1 cells. Monocytes differentiate into M1-type macrophages in response to IFN- γ or M2-type macrophages in response to IL-10. M1-type macrophages can also transform into M2-type macrophages in response to TGF- β or M-CSF, and conversely, M2-type macrophages can transform into M1-type macrophages in response to IL-12 or TNF- α . Tumor cells can exert immunosuppressive effects by connecting PD-L1 on their surface to PD-1 on the surface of T cells. In contrast, T cells also trigger an immune response by contacting and killing tumor cells. In the figure, the thick black solid lines indicate cell-cell interactions, such as cell differentiation and antigen presentation; the thin black dotted lines indicate positive cytokine-related effects, such as cytokine production, promotion of cell proliferation, and promotion of cell differentiation; and the thin red dotted lines indicate cytokine-related inhibitory effects, such as inhibition of cell proliferation and inhibition of cell differentiation (Color figure online)

(Lawrence and Natoli 2011; Noy and Pollard 2014; Mosser and Edwards 2008). The variables of the model are listed in Table 1.

In this study, we developed a model using ordinary differential equations (ODEs) to understand how different parts of the tumor microenvironment interact with each other, based on the dynamic regulatory network shown in Fig. 1. The ODEs model was designed to present both rapid and slow changes in the tumor microenvironment. Rapid changes relate to variations in cytokine concentrations at the molecular level, while slow changes pertain to shifts in the number of cell populations at the cell level. To simulate the concentration dynamics of small molecule proteins such as cytokines

Table 1 List of variables

Variate	Description	Unit
D	The number of dendritic cells	cells
C	The number of tumor cells	cells
T_1	The number of activated CD4 $^{+}$ T cells	cells
T_8	The number of activated CD8 $^{+}$ T cells	cells
T_r	The number of activated Treg cells	cells
M_1	The number of type 1 macrophages	cells
M_2	The number of type 2 macrophages	cells
I_2	IL-2 concentration	ng mL $^{-1}$
I_{12}	IL-12 concentration	ng mL $^{-1}$
I_{10}	IL-10 concentration	ng mL $^{-1}$
T_{β}	TGF- β concentration	ng mL $^{-1}$
I_{γ}	IFN- γ concentration	ng mL $^{-1}$
T_{α}	TNF- α concentration	ng mL $^{-1}$
M_c	M-CSF concentration	ng mL $^{-1}$
P	PD-1 concentration	nmol L $^{-1}$
L	PD-L1 concentration	nmol L $^{-1}$
A	Anti-PD-1 concentration	nmol L $^{-1}$
B	FGFR inhibitor concentration	nmol L $^{-1}$

at the molecular level, we have incorporated production and degradation rates. For biological systems at the cellular level, we have used the Michaelis-Menten function to model changes in the number of cell populations. In addition, considering that proteins such as cytokines undergo production, degradation, binding, and dissociation much faster than changes in cell phenotype and population size, we introduced a proposed quasi-steady-state assumption to capture the dynamics of cytokine concentrations. This assumption can be integrated into the cellular level to regulate changes in cell population size, thereby linking these two different biological scales.

2.1.1 Cell Level: Dynamic Changes in Cell Numbers

Equation for Dendritic Cells (D)

Tumor cells activate immature dendritic cells (D_0), transforming them into activated dendritic cells (D) by releasing tumor-associated antigens (TAA). Activated dendritic cells can effectively perform antigen presentation and activate various types of immune cells, initiating an immune response (Wculek et al. 2020). We assumed a constant number of immature dendritic cells (D_0), and the activation rate of D_0 is proportional to the TAA concentration, which depends on tumor cell number C through a Michaelis-Menten function. The dynamics of D is represented as follows:

$$\frac{dD}{dt} = \underbrace{\lambda_{DC} \frac{C}{K_C + C} D_0}_{\text{activation by tumor}} - \underbrace{d_D D}_{\text{death}}. \quad (1)$$

Here, λ_{DC} represents the activation rate of dendritic cells by tumor cells, K_C is the half-saturation constant for tumor cells, and d_D is the apoptosis rate of dendritic cells.

Equation for CD4⁺T Cells (T_1)

Naive CD4⁺T cells differentiate into Th1 cells (T_1) in response to IL-12 (Trinchieri 2003), and this process is inhibited by IL-10 and TGF- β (Mosser and Zhang 2008; Tripathi and Lahesmaa 2014). Moreover, T_1 cells can promote their own proliferation through autocrine IL-2 (Spolski et al. 2018). During the activation and proliferation of T_1 cells, bladder cancer cells exert immunosuppressive effects by binding PD-L1 (L) to PD-1 (P) on the surface of T_1 cells (Kim and Chen 2016). Therefore, T_1 satisfies the following equation:

$$\frac{dT_1}{dt} = \left(\underbrace{\lambda_{T_1 I_{12}} T_{10} \frac{I_{12}}{K_{I_{12}} + I_{12}}}_{\text{activation by IL-12}} \times \underbrace{\frac{1}{1 + I_{10}/K_{I_{10}}} \times \frac{1}{1 + T_\beta/K_{T_\beta}}}_{\text{inhibition by IL-10 and TGF-}\beta} + \underbrace{\lambda_{T_1 I_2} T_1 \frac{I_2}{K_{I_2} + I_2}}_{\text{proliferation by IL-2}} \right) \times \underbrace{F(P, L, A)}_{\text{inhibition by PD-1-PD-L1}} - \underbrace{d_{T_1} T_1}_{\text{death}}. \quad (2)$$

Here, $\lambda_{T_1 I_{12}}$ is the activation rate of IL-12 on CD4⁺T cells, T_{10} is naive CD4⁺T cells, $K_{I_{12}}$, $K_{I_{10}}$, K_{T_β} , K_{I_2} are the half-saturation of IL-12, IL-10, TGF- β and IL-2, respectively, $\lambda_{T_1 I_2}$ is the appreciation rate of IL-2-mediated of CD4⁺T cells, d_{T_1} is the apoptosis rate of CD4⁺T cells, and $F(P, L, A)$ is the immunosuppression function of the PD-1-PD-L1 ligation process under the action of immune checkpoint inhibitor (A). For details on the expression, see Sect. 2.2.1 and “Appendix A.1”.

Equation for CD8⁺T Cells (T_8)

Naive CD8⁺T cells differentiate into CTL cells (T_8) in response to IL-12 (Trinchieri 2003), while IL-10 and TGF- β in the tumor microenvironment play an inhibitory role in this process (Mosser and Zhang 2008; Tripathi and Lahesmaa 2014; Smith et al. 2018). On the other hand, IL-2 secreted by T_1 cells promotes the proliferation of T_8 cells (Spolski et al. 2018). Like the activation and proliferation process of T_1 cells, the PD-1-PD-L1 pathway continues to play an immunosuppressive role (Kim and Chen

2016). Hence T_8 satisfies the following equation:

$$\frac{dT_8}{dt} = \left(\underbrace{\lambda_{T_8 I_{12}} T_{80} \frac{I_{12}}{K_{I_{12}} + I_{12}}}_{\text{activation by IL-12}} \times \underbrace{\frac{1}{1 + I_{10}/K_{I_{10}}} \times \frac{1}{1 + T_\beta/K_{T_\beta}}}_{\text{inhibition by IL-10 and TGF-}\beta} + \underbrace{\lambda_{T_8 I_2} T_8 \frac{I_2}{K_{I_2} + I_2}}_{\text{proliferation by IL-2}} \right) \\ \times \underbrace{F(P, L, A)}_{\text{inhibition by PD-1-PD-L1}} - \underbrace{d_{T_8} T_8}_{\text{death}}, \quad (3)$$

where $\lambda_{T_8 I_{12}}$ is the activation rate of CD8⁺T cells by IL-12, T_{80} is the number of naive CD8⁺T cells, $\lambda_{T_8 I_2}$ is the appreciation rate of IL-2-mediated of CD8⁺T cells, and d_{T_8} is the apoptosis rate of CD8⁺T cells.

Equation for Treg Cells (T_r)

Regulatory T cells (T_r) are one of the most important factors in the maintenance of immune tolerance. Foxp3 is a key transcription factor for Treg. TGF- β promotes the up-regulation of Foxp3, accelerating the production of T_r (Chen et al. 2003), and this process is inhibited by IFN- γ (Ulloa et al. 1999). Thus, we obtain the following equation for T_r :

$$\frac{dT_r}{dt} = \underbrace{\lambda_{T_r T_\beta} T_{10} \frac{T_\beta}{K_{T_\beta} + T_\beta}}_{\text{activation by TGF-}\beta} \times \underbrace{\frac{1}{1 + I_\gamma/K_{I_\gamma}}}_{\text{inhibition by IFN-}\gamma} - \underbrace{d_{T_r} T_r}_{\text{death}}, \quad (4)$$

where $\lambda_{T_r T_\beta}$ is the activation rate of Treg by TGF- β , K_{I_γ} is the half-saturation of IFN- γ , and d_{T_r} is the apoptosis rate of Treg cells.

Equations for M1-Type (M_1) and M2-Type (M_2) Macrophages

In the tumor microenvironment, monocytes (M) can differentiate into M1-type macrophages in response to IFN- γ , or into M2-type macrophages in response to IL-10 (Lawrence and Natoli 2011). The two macrophage phenotypes are not fixed, and there is a complex phenotypic transformation between them. M-CSF and TGF- β secreted by tumor cells promote the transformation of M1-type macrophages to M2-type macrophages, whereas IL-12 and TNF- α play the opposite role by promoting the transformation of M2-type macrophages to M1-type macrophages (Lawrence and Natoli 2011; Noy and Pollard 2014; Mosser and Edwards 2008). Thus, we have the model equations

$$\frac{dM_1}{dt} = \underbrace{\lambda_{M I_\gamma} M \frac{I_\gamma}{K_{I_\gamma} + I_\gamma}}_{\text{polarization by IFN-}\gamma} + \underbrace{\beta_2 M_2 \left(\frac{I_{12}}{K_{I_{12}} + I_{12}} + \frac{T_\alpha}{K_{T_\alpha} + T_\alpha} \right)}_{\text{M2}\rightarrow\text{M1 by IL-12 and TNF-}\alpha}$$

$$-\underbrace{\beta_1 M_1 \left(\frac{T_\beta}{K_{T_\beta} + T_\beta} + \frac{M_c}{K_{M_c} + M_c} \right)}_{\text{M1} \rightarrow \text{M2 by M-CSF and TGF-}\beta} - \underbrace{d_{M_1} M_1}_{\text{death}}, \quad (5)$$

and

$$\begin{aligned} \frac{dM_2}{dt} = & \underbrace{\lambda_{M I_{10}} M \frac{I_{10}}{K_{I_{10}} + I_{10}}}_{\text{polarization by IL-10}} + \underbrace{\beta_1 M_1 \left(\frac{T_\beta}{K_{T_\beta} + T_\beta} + \frac{M_c}{K_{M_c} + M_c} \right)}_{\text{M1} \rightarrow \text{M2 by M-CSF and TGF-}\beta} \\ & - \underbrace{\beta_2 M_2 \left(\frac{I_{12}}{K_{I_{12}} + I_{12}} + \frac{T_\alpha}{K_{T_\alpha} + T_\alpha} \right)}_{\text{M2} \rightarrow \text{M1 by IL-12 and TNF-}\alpha} - \underbrace{d_{M_2} M_2}_{\text{death}}, \end{aligned} \quad (6)$$

where $\lambda_{M I_\gamma}$ is the polarization rate of IFN- γ to monocytes, $\lambda_{M I_{10}}$ is the polarization rate of IL-10 to monocytes, β_1 is the transformation rate of M1-type macrophages to M2-type macrophages, β_2 is the transformation rate of M2-type macrophages to M1-type macrophages, K_{T_α} and K_{M_c} are the half-saturation of TNF- α and M-CSF, respectively, d_{M_1} is the apoptosis rate of M1-type macrophages, and d_{M_2} is the apoptosis rate of M2-type macrophages.

Equation for Tumor Cells (C)

The excessive proliferation of bladder cancer cells is primarily linked to the overactivation of fibroblast growth factor receptor (FGFR) on the surface (Katoh 2019; Rozen 2020). This paper presents a novel tumor growth model that characterizes tumor proliferation based on the activation ratio of FGFR on the cell surface. The equation is expressed as follows:

$$\frac{dC}{dt} = \underbrace{\lambda(C) \cdot C}_{\text{tumor growth}} - \underbrace{(\eta_1 T_1 + \eta_8 T_8) \cdot C}_{\text{apoptosis of tumor by T}_1 \text{ and T}_8} - \underbrace{d_C C}_{\text{death}}, \quad (7)$$

where $\lambda(C)$ represents the proliferation rate determined by the proportion of the activated state FGFR on the tumor cell surface, as a function of tumor cell dependence, η_1 and η_8 are the killing rates of T_1 and T_8 on tumor cells, respectively, and d_C is the apoptosis rate of bladder cancer cells. For detailed expressions of the proliferation rate $\lambda(C)$, refer to Sect. 2.2.2 and “Appendix A.2”.

2.1.2 Cytokine Level: Dynamic Changes in Protein Concentrations

Equation for IL-12 (I_{12})

IL-12, a cytokine with diverse biological activities, is predominantly secreted by dendritic cells (D) (Trinchieri 2003) and M1-type macrophages (M_1) (Lawrence and

Natoli 2011). Therefore,

$$\frac{dI_{12}}{dt} = \underbrace{\delta_{I_{12}D} D}_{\text{production by DC}} + \underbrace{\delta_{I_{12}M_1} M_1}_{\text{production by M1}} - \underbrace{d_{I_{12}} I_{12}}_{\text{degradation}}, \quad (8)$$

where $\delta_{I_{12}D}$ is the production rate of IL-12 by dendritic cells, $\delta_{I_{12}M_1}$ is the production rate of IL-12 by M1-type macrophages, and $d_{I_{12}}$ is the degradation rate of IL-12.

Equation for IL-2 (I_2)

IL-2, a cytokine promoting lymphocyte proliferation and differentiation, crucial in the immune response, is produced by activated CD4⁺T cells (T_1) (Spolski et al. 2018). Therefore,

$$\frac{dI_2}{dt} = \underbrace{\delta_{I_2 T_1} T_1}_{\text{production by } T_1} - \underbrace{d_{I_2} I_2}_{\text{degradation}}, \quad (9)$$

where $\delta_{I_2 T_1}$ is the production rate of IL-2 by CD4⁺T cells, and d_{I_2} is the degradation rate of IL-2.

Equation for IFN- γ (I_γ)

The pro-inflammatory cytokine IFN- γ , the only member of the II type interferon, is primarily produced by activated CD4⁺T cells (T_1) (Tripathi and Lahesmaa 2014) and CD8⁺T cells (T_8) (Decker et al. 2005). The equation is given by

$$\frac{dI_\gamma}{dt} = \underbrace{\delta_{I_\gamma T_1} T_1}_{\text{production by } T_1} + \underbrace{\delta_{I_\gamma T_8} T_8}_{\text{production by } T_8} - \underbrace{d_{I_\gamma} I_\gamma}_{\text{degradation}}, \quad (10)$$

where $\delta_{I_\gamma T_1}$ is the production rate of IFN- γ by CD4⁺T cells, $\delta_{I_\gamma T_8}$ is the production rate by CD8⁺T cells, and d_{I_γ} is the degradation rate.

Equation for TNF- α (T_α)

TNF- α , the first cytokine used in tumor therapy, is primarily produced by activated CD4⁺T cells (T_1) (Balkwill 2009), CD8⁺T cells (T_8) (Balkwill 2009), and M1-type macrophages (Lawrence and Natoli 2011; Balkwill 2009). The equation is given by

$$\frac{dT_\alpha}{dt} = \underbrace{\delta_{T_\alpha T_1} T_1}_{\text{production by } T_1} + \underbrace{\delta_{T_\alpha T_8} T_8}_{\text{production by } T_8} + \underbrace{\delta_{T_\alpha M_1} M_1}_{\text{production by M1}} - \underbrace{d_{T_\alpha} T_\alpha}_{\text{degradation}}, \quad (11)$$

where $\delta_{T_\alpha T_1}$ is the production rate of TNF- α by CD4⁺T cells, $\delta_{T_\alpha T_8}$ is the production rate by CD8⁺T cells, $\delta_{T_\alpha M_1}$ is the production rate by M1-type macrophages, and d_{T_α} is the degradation rate.

Equation for TGF- β (T_β)

TGF- β , a multifunctional cytokine regulating many signaling pathways, is primarily produced by tumor cells (C) (Battie and Massagué 2019), Treg (T_r) (Battie and Massagué 2019), and M2-type macrophages (M_2) (Mosser and Edwards 2008). The equation is given by

$$\frac{dT_\beta}{dt} = \underbrace{\delta_{T_\beta C} C}_{\text{production by tumor}} + \underbrace{\delta_{T_\beta T_r} T_r}_{\text{production by Treg}} + \underbrace{\delta_{T_\beta M_2} M_2}_{\text{production by M2}} - \underbrace{d_{T_\beta} T_\beta}_{\text{degradation}}, \quad (12)$$

where $\delta_{T_\beta C}$ is the production rate of TGF- β by tumor cells, $\delta_{T_\beta T_r}$ is the production rate by Treg cells, $\delta_{T_\beta M_2}$ is the production rate by M2-type macrophages, and d_{T_β} is the degradation rate.

Equation for M-CSF (M_c)

Macrophage colony-stimulating factor (M-CSF), also known as colony-stimulating factor-1 (CSF-1), is a lineage-specific cytokine and is mainly produced by tumor cells (C) (Karagiannidis et al. 2021). The equation is given by

$$\frac{dM_c}{dt} = \underbrace{\delta_{M_c C} C}_{\text{production by tumor}} - \underbrace{d_{M_c} M_c}_{\text{degradation}}, \quad (13)$$

where $\delta_{M_c C}$ is the production rate of M-CSF by tumor cells, and d_{M_c} is the degradation rate of M-CSF.

Equation for IL-10 (I_{10})

The anti-inflammatory cytokine IL-10, which plays a crucial role in immunomodulatory, is mainly produced by tumor cells (C) (Khong and Restifo 2002), Treg (T_r) (Rubtsov et al. 2008), and M2-type macrophages (M_2) (Mosser and Edwards 2008). The equation is given by

$$\frac{dI_{10}}{dt} = \underbrace{\delta_{I_{10} C} C}_{\text{production by tumor}} + \underbrace{\delta_{I_{10} T_r} T_r}_{\text{production by Treg}} + \underbrace{\delta_{I_{10} M_2} M_2}_{\text{production by M2}} - \underbrace{d_{I_{10}} I_{10}}_{\text{degradation}}, \quad (14)$$

where $\delta_{I_{10} C}$ is the production rate of IL-10 by tumor cells, $\delta_{I_{10} T_r}$ is the production rate by Treg cells, $\delta_{I_{10} M_2}$ is the production rate M2-type macrophages, and $d_{I_{10}}$ is the degradation rate.

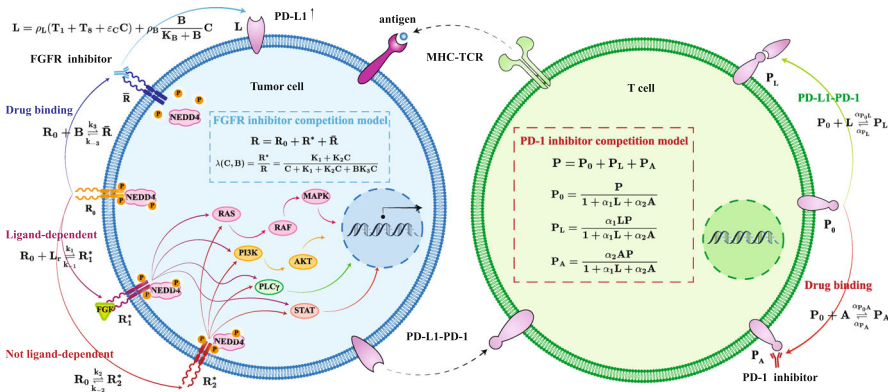


Fig. 2 Mechanism diagram of the target competition model. The left panel illustrates the change in FGFR on the surface of tumor cells with four different states, while the right panel illustrates the changes in PD-1 on effector T cells. On the surface of tumor cells, FGFR undergoes changes in four states: mutant free-state receptor (R_0), ligand-dependent activated-state receptor (R^*), ligand-independent activated-state receptor (R_1^*), or drug-bound closed-state receptor (\bar{R}). Simultaneously, PD-1 on effector T cells exhibits three states: free-state PD-1 (P_0), PD-1-PD-L1 complex (P_L), or PD-1-anti-PD-1 complex (P_A). FGFR and PD-1 inhibitors work together to modulate the competition between different states (color figure online)

2.2 Mathematical Model of the Competitive Mechanism of Ligand or Drug Binding to the Receptor

The competition mechanism for ligand or drug binding to the receptor is commonly described by the target competition model. The drug's collective binding site is known as the drug target, and receptors, ion channels, gene loci, and transporters are typical drug targets (Rosenbaum et al. 2020). Receptors, which are a class of functional proteins that mediate cellular signaling, are the primary and most important drug targets. They display high selectivity and affinity when recognizing and binding ligands or targeted drugs (Rosenbaum et al. 2020). Notable receptor types include PD-1 (Tumeh et al. 2014), PD-L1 (Yamaguchi et al. 2022), HER2 (Friedlaender et al. 2022), VEGF (Goel and Mercurio 2013), FGFR (Katoh 2019), and EGFR (Friedlaender et al. 2022). Representative drugs for these receptors include Nivolumab, Atezolizumab, Trastuzumab, Ranibizumab, Erdafitinib, and Gefitinib.

The competitive binding processes are depicted in Fig. 2 and can be characterized using a chemical rate equation. FGFR on the surface of tumor cells undergoes changes in four states: mutant free-state receptor, ligand-dependent activated-state receptor, ligand-independent activated-state receptor, or drug-bound closed-state receptor. Meanwhile, PD-1 on effector T cells exhibits three states: free-state PD-1, PD-1-PD-L1 complex, or PD-1-anti-PD-1 complex. FGFR and PD-1 inhibitors work together to modulate the competition between different states. The target competition model for anti-PD-1 and anti-FGFR was derived based on the quasi-steady-state assumption and the law of mass conservation. The mathematical formulation and biological mechanisms of the specific chemical reactions are detailed in “Appendix A”.

2.2.1 Target Competition Model of Immune Checkpoint Inhibitor (Anti-PD-1)

Programmed death ligand 1 (PD-L1) is expressed on the surface of T_1 and T_8 cells (Walshaw et al. 2018; Keir et al. 2008). We denote the expression rate of PD-L1 on these cells as ρ_L . Additionally, bladder cancer cells highly express PD-L1 on their cell surface (Schneider et al. 2019; Keir et al. 2008). The PD-L1 expression is regulated by a parameter ε_T whose exact value is determined according to the type of cancer. Meanwhile, FGFR inhibitors promote the expression of PD-L1 on the surface of tumor cells (Jing et al. 2022), the equation governing the concentration of PD-L1 on the cell surface is given by:

$$L = \rho_L (T_1 + T_8 + \varepsilon_C C) + \rho_B \frac{B}{K_B + B} C, \quad (15)$$

where ρ_B is the expression rate of PD-L1 on the surface of the tumor cell induced by the FGFR inhibitor, and K_B is the half-saturation of the FGFR inhibitor.

Simultaneously, programmed death receptor 1 (PD-1) is predominantly expressed on activated T_1 and T_8 cells (Schneider et al. 2019), with the expression rate denoted as ρ_P . The equation for the concentration of PD-1 is expressed as:

$$P = \rho_P (T_1 + T_8). \quad (16)$$

Under the influence of immune checkpoint inhibitors (ICIs) (Fig. 2), the immuno-suppression function is defined as:

$$F(P, L, A) = \frac{1}{1 + P_L/K_P}, \text{ where } P_L = \frac{\alpha_1 L P}{1 + \alpha_1 L + \alpha_2 A}. \quad (17)$$

Here, K_P is the immune checkpoint inhibition constant, P_L is the concentration of the PD-1-PD-L1 complex, and α_1 and α_2 are the equilibrium constants for the binding process of P_0 to PD-L1 and anti-PD-1, respectively. The details are described in the derivation of the process in “Appendix A.1”.

Given the prolonged action of anti-PD-1, typically administered every 3 days, the concentration change equation of PD-1 inhibitors is given by:

$$\frac{dA}{dt} = \hat{A}(t) - d_A A, \quad (18)$$

where d_A is the consumption rate of anti-PD-1 and $\hat{A}(t)$ is the administration rate given by a segmented function dependent on time t :

$$\hat{A}(t) = \begin{cases} \gamma_A \times \frac{1}{T}, & 3k \leq t < 3k + T \\ 0, & 3k + T \leq t < 3(k+1) \end{cases}, \quad k = 0, 1, 2, \dots, 7. \quad (19)$$

Here, γ_A represents the injection dose of anti-PD-1, and T is the time period of drug injection ($T < 1$). We assumed that the drug is administrated daily, and for each drug injection lasting the duration T , the total daily dose is $\gamma_A \times \frac{1}{T} \times T = \gamma_A$.

2.2.2 Target Competition Model of Targeted Inhibitors (Anti-FGFR)

Activating mutations in FGFR is a common feature of bladder cancer, leading to an enhanced binding affinity between FGF and FGFR, as well as ligand-independent receptor dimerization (Katoh 2019; Babina and Turner 2017; Acevedo et al. 2009; van Kessel et al. 2015). The activating mutations in FGFR, present on the surface of bladder cancer cells, have two effects. Firstly, the ligand-receptor binding strength is enhanced to accelerate tumor proliferation signaling. Secondly, the downstream signaling pathways are activated in a ligand-independent pathway to regulate tumor proliferation. The tumor proliferation mediated by FGFR occurs in three different ways, as shown in Fig. 2. The first way is when the mutant free-state receptor (R_0) binds to a ligand (L_r) and forms a ligand-dependent activated-state receptor (R_1^*), which then activates the signaling pathway leading to tumor growth. The second way occurs when the mutant free-state receptor does not require the presence of the ligand and forms a ligand-independent activated-state receptor (R_2^*), which also activates the signaling pathway for tumor growth. Finally, the third way is when the mutant free-state receptor binds to an FGFR inhibitor (B) to form a drug-binding closed-receptor (\bar{R}), thus blocking the signaling pathway and inhibiting tumor growth.

Based on the above mechanism, the proliferation rate of tumor cells in response to targeted inhibitors is expressed as:

$$\lambda(C, B) = \theta_C \times \frac{R^*}{R} = \theta_C \times \frac{K_1 + K_2 C}{C + K_1 + K_2 C + K_3 B C}, \quad (20)$$

where θ_C denotes the maximum proliferation rate of tumor cells, R^*/R is the activated-state receptor percentage or called partial saturation, R^* is the activated-state receptor concentration, R is the total receptor concentration, K_1 , K_2 , and K_3 are equilibrium constants for ligand-dependent activation process, ligand-independent activation process, and drug-binding closure process, respectively. For a detailed derivation of the equation, please refer to “Appendix A.2”.

Additionally, the equation for the concentration change of FGFR inhibitors is given as:

$$\frac{dB}{dt} = \hat{B}(t) - d_B B, \quad (21)$$

where d_B is the consumption rate of anti-FGFR, and $\hat{B}(t)$ is the administration rate, defined as a segmented function dependent on time t :

$$\hat{B}(t) = \begin{cases} \gamma_B \times \frac{1}{T}, & k \leq t < k + T \\ 0, & k + T \leq t < k + 1 \end{cases}, \quad k \in [3, 21]. \quad (22)$$

Here, γ_B is the injection dose of anti-FGFR, T is the time period of drug injection ($T < 1$).

The proposed model integrates key elements in the competitive binding of ligands or drugs to receptors and provides a comprehensive framework for understanding the dynamics of immune checkpoint inhibitors and targeted inhibitors in the context of tumor growth.

2.3 Parameter Estimation

The mathematical model contains seven classes of tumor immune-related parameters. To estimate the parameters in the dynamical model, we first determined the order of magnitude of different parameter types referring to published literature. We referred to Chen and Lai (2022) for the magnitude of naive immune cells in the tumor microenvironment of about 10^7 – 10^9 cells. For the cytokine activation rate and polarization rate λ_{xy} , we referred to Chen and Lai (2022) and Lai et al. (2018), which give the magnitude of 10^0 – 10^1 day $^{-1}$. We referred to Lai et al. (2018) for the polarization rates β_x , which gives the magnitude of 10^{-3} – 10^{-1} day $^{-1}$. For the apoptosis rates d_x of immune cells and the half-saturation of cytokines K_x , we referred to several studies (Lai and Friedman 2017a; Lai et al. 2018; Friedman and Hao 2018; Li et al. 2022) for the magnitude of d_x of about 10^{-1} day $^{-1}$, and the magnitude of K_x of about 10^{-2} – 10^1 ng mL $^{-1}$. For the cytokine production rate δ_{xy} , we referred to Robertson-Tessi et al. (2012), which gives the magnitude between 10^{-7} and 10^{-10} ng mL $^{-1}$ day $^{-1}$ cell $^{-1}$. The apoptosis rate of cytokines d_y was obtained using the half-life as $d_y = \frac{\ln 2}{t_{1/2}}$, where $t_{1/2}$ represents the half-life of the cytokine. For other parameters related to tumor cells and drug therapy, the approximate magnitudes were estimated based on related references from Jing et al. (2022), Lai and Friedman (2017a), Lai et al. (2018); Friedman and Hao (2018), Storey et al. (2020), Okuneye et al. (2021). The order of magnitudes of the parameters is listed in Table 2. Finally, the exact parameter values were adjusted based on the Markov chain Monte Carlo method (MCMC) and were identified in accordance with the biological roles of specific parameters in the equations. For details, refer to “Appendix C”.

2.4 Numerical Scheme

The Fourth-order Runge–Kutta (FRK) method was used to solve the proposed mathematical model, which integrates the drug target competition with the multiscale tumor microenvironment model. We used published mathematical models (Lai et al. 2018; Lai and Friedman 2017a; Li et al. 2022; Robertson-Tessi et al. 2012; Storey et al. 2020; Lui et al. 2002; Mueller et al. 2009; Saxena et al. 2015; Friedman and Hao 2018; Foon et al. 1985; Oliver et al. 1993; Johnson et al. 2016) to estimate the parameters, and then the Markov chain Monte Carlo (MCMC) method was employed to determine the final parameter values based on real experimental data (Jing et al. 2022). Following the local sensitivity analysis (LSA) results, we utilized the random sampling (RS) method to extract parameter combinations within the specified value space of the tumor heterogeneity parameter. This allowed us to generate parameters for virtual experimental mice in our study. Then, we performed survival analysis (SA), kernel density estimation (KDE), and chord diagram analysis (CDA) to evaluate different treatment options. The computational framework is summarized in Fig. 3.

We developed a discrete cellular automata (CA) model to study the dynamic process of tumor progression. This model consists of multiple individual cells and mimics various life processes, leading to complex macroscopic systems with different behaviors. The flowchart of cellular automata is shown in Fig. 4. In CA, we simulated the

Table 2 Parameter sets and corresponding order of magnitudes

Set	Corresponding parameters	Magnitude	Unit	References
Cell	D_0, T_{10}, T_{80}, M	$10^7\text{--}10^9$	cells	Chen and Lai (2022)
λ_{xy}	$\lambda_{DC}, \lambda_{T_1 I_{12}}, \lambda_{T_8 I_{12}}, \lambda_{T_1 I_2}$ $\lambda_{T_8 I_2}, \lambda_{T_r T_\beta}, \lambda_{M I_\gamma}, \lambda_{M I_{10}}$	$10^0\text{--}10^1$	day $^{-1}$	Chen and Lai (2022) Lai et al. (2018)
β_x	β_1, β_2	$10^{-3}\text{--}10^{-1}$	day $^{-1}$	Lai et al. (2018)
d_x	$d_D, d_{T_1}, d_{T_8}, d_{T_r}, d_{M_1}, d_{M_2}$	10^{-1}	day $^{-1}$	Li et al. (2022) Friedman and Hao (2018)
K_x	$K_{I_2}, K_{I_{12}}, K_{I_{12}}, K_{T_\beta}$ $K_{I_\gamma}, K_{T_\alpha}, K_{M_c}$	$10^{-2}\text{--}10^1$	ng mL $^{-1}$	Li et al. (2022) Lai and Friedman (2017a) Lai et al. (2018) Friedman and Hao (2018)
δ_{xy}	$\delta_{I_{12}} D, \delta_{I_{12}} M_1, \delta_{I_2} T_1, \delta_{I_\gamma} T_1, \delta_{I_\gamma} T_8$ $\delta_{T_\alpha} T_1, \delta_{T_\alpha} T_8, \delta_{T_\alpha} M_1, \delta_{T_\beta} C, \delta_{T_\beta} T_r$ $\delta_{T_\beta} M_2, \delta_{M_C} C, \delta_{I_{10}} C, \delta_{I_{10}} T_r, \delta_{I_{10}} M_2$	$10^{-7}\text{--}10^{-10}$	ng mL $^{-1}$ day $^{-1}$ cell $^{-1}$	Robertson-Tessi et al. (2012)
d_y	$d_{I_{12}}, d_{I_{10}}, d_{I_2}, d_{I_\gamma}, d_{T_\alpha}, d_{T_\beta}, d_{M_c}$	$10^0\text{--}10^2$	day $^{-1}$	Lai et al. (2018) Lui et al. (2002) Mueller et al. (2009) Saxena et al. (2015) Friedman and Hao (2018) Foon et al. (1985) Oliver et al. (1993) Johnson et al. (2016)

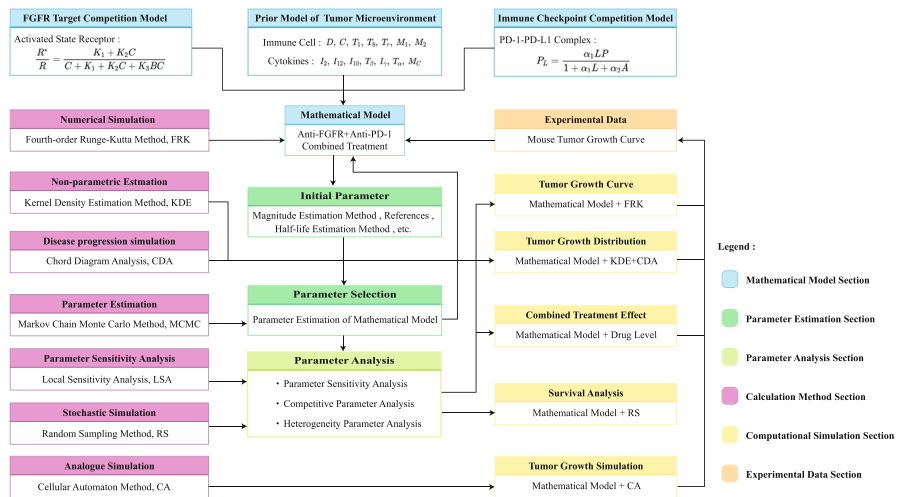


Fig. 3 Illustration of the computational framework (color figure online)

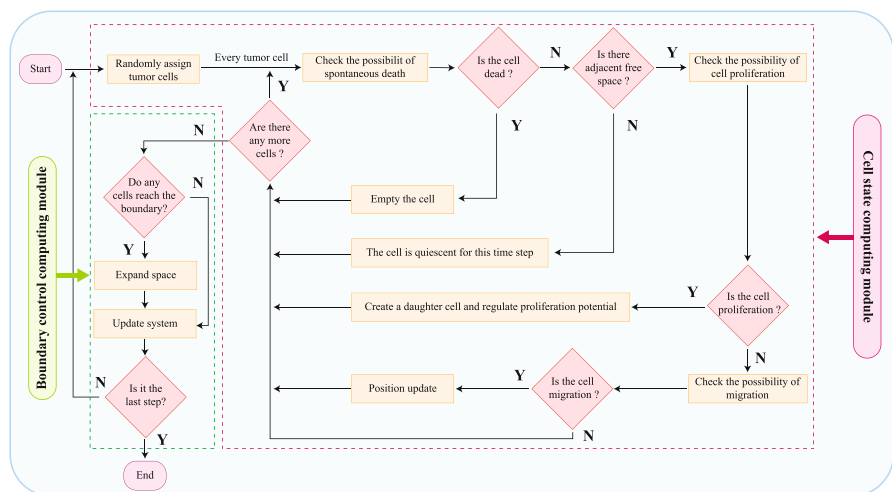


Fig. 4 Flowchart of cellular automata algorithm (color figure online)

behavior of individual cells (proliferation, migration, apoptosis, or quiescence) and used Poisson's process to determine the cell fate at each time step, based on the proposed mathematical model. Specifically, we simulated the dynamic growth of tumors under four different administration conditions and presented the experimental results visually.

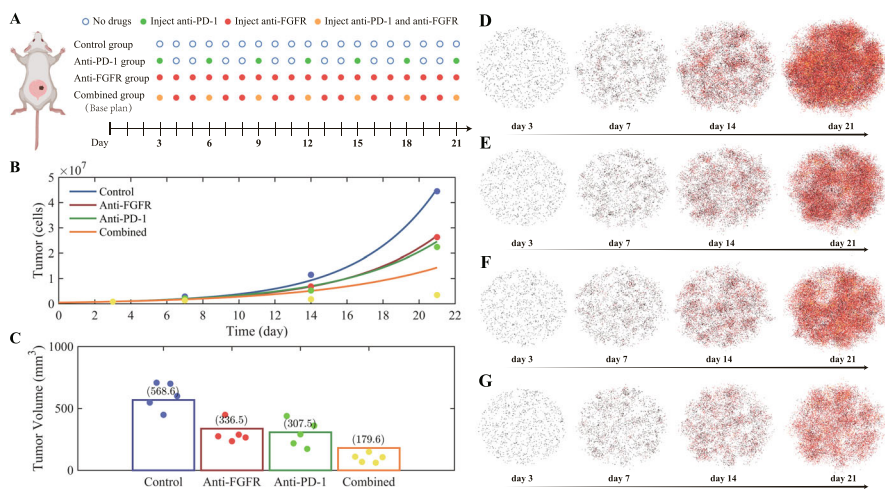


Fig. 5 Simulating tumor evolution under different therapeutic modalities. **A** Dosing regimen of the control group, anti-PD-1 group, anti-FGFR group, and combined group. **B** Time course of simulated tumor evolution. The points represent the average of experimental data. **C** Tumor volume at day 21. The dots represent experimental data, and the bars represent simulated data; see “Appendix B”. **D–G** Tumor evolution dynamics for the control group (**D**), anti-FGFR group (**E**), anti-PD-1 group (**F**), and combination therapy group (**G**) using the cellular automata method. The color of cells represents the cell proliferation ability, with darker colors indicating stronger cell proliferation ability and lighter colors indicating weaker cell proliferation ability (color figure online)

3 Results

3.1 Tumor Growth Simulation and Model Validation Under Different Treatments

The baseline data for tumor evolution originated from an experiment involving the injection of C57BL/6 mice with the MB49 cancer cell line (Jing et al. 2022). This experiment investigated the therapeutic efficacy of bladder cancer using FGFR or PD-1 inhibitors alone, or combination therapy with both types of inhibitors. Tumor development was monitored through the fluorescence imaging system, and tumor volume was measured at the experiment’s endpoint. To comprehensively explore the tumor evolution process under distinct therapeutic modalities, we integrated the target competition model into the mathematical model of the tumor microenvironment dynamics, providing a realistic depiction of the changes in tumor burden in mice.

We simulated tumor evolution under different therapeutic modalities for model calibration and validation and compared the results with experimental data (Jing et al. 2022). Four virtual experimental groups were established based on the experimental setup: control group, anti-PD-1 group, anti-FGFR group, and combination group. Immune checkpoint inhibitors were administered every three days, while targeted inhibitors were administered daily, as illustrated in Fig. 5A. Notably, applying anti-PD-1 or anti-FGFR alone can reduce tumor growth compared to the control group, and a combination of the two drugs exhibited superior efficacy in repressing tumor growth (Fig. 5B). These findings were further corroborated by tumor volume data on

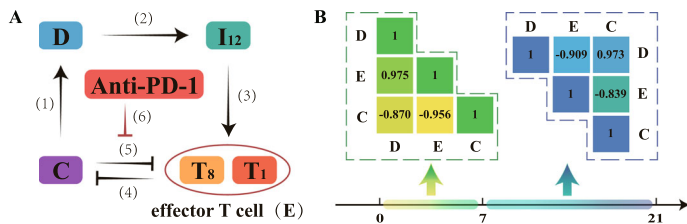


Fig. 6 Key regulatory mechanisms of the tumor microenvironment. **A** Key regulatory mechanisms of tumor microenvironment delineated by tumor cells (C), dendritic cells (D), and effector T cells (E). **B** Correlation analysis between tumor cells (C), dendritic cells (D), and effector T cells (E) at days 0–7 and 7–21, respectively (color figure online)

day 21 (Fig. 5C). Additionally, we conducted computational simulations to study how tumor cells behave using cellular automata. The simulations took into account cell proliferation, apoptosis, migration, and quiescence (Fig. 4). Simulations showed that combination therapy markedly decreased tumor density, as demonstrated in Fig. 5D–G. The numerical results are consistent with mouse experiments (Jing et al. 2022), confirming the accuracy of our mathematical model in depicting the tumor evolution pattern during therapy.

We use the root mean square error (RMSE) to quantify the fitting between model simulation and real data as follows:

$$RMSE = \sqrt{\frac{1}{n} \sum_{i=1}^n (x_i - \hat{x}_i)^2},$$

where x_i means the experimental data (tumor volume) and \hat{x}_i represents the corresponding simulated value. The RMSE values of the control group, anti-FGFR group, anti-PD-1 group, and combined group are 15.9269 mm^3 , 4.1210 mm^3 , 17.4153 mm^3 , and 70.7241 mm^3 , respectively. The results indicate that model simulation can capture the dynamic evolution of tumors well under different treatment schemes. The RMSD for the combined therapy group is larger than other groups, which may be attributed to the less obvious response of smaller tumor populations in fluorescence instruments.

3.2 Key Regulatory Pathways and Tumor Microenvironment Evolution

The regulatory network diagram in Fig. 1 outlines the key components governing tumor growth, including activated dendritic cells performing antigen presentations and effector T cells (T_1 and T_8) responsible for tumor cell elimination. Tumor cells also play an immunosuppressive role by forming the PD-1-PD-L1 complex (Fig. 6A). To quantify the relationships between different cell numbers during tumor growth with anti-PD-1 treatment, we conducted a correlation analysis between the numbers of tumor cells (C), dendritic cells (D), and effector T cells (E). The correlation coefficients, depicted in Fig. 6B, reveal dynamic correlations during different periods.

At the early stage (days 0–7), the dendritic and effector cell numbers exhibit a high positive correlation (0.975). In contrast, the correlation becomes highly negative

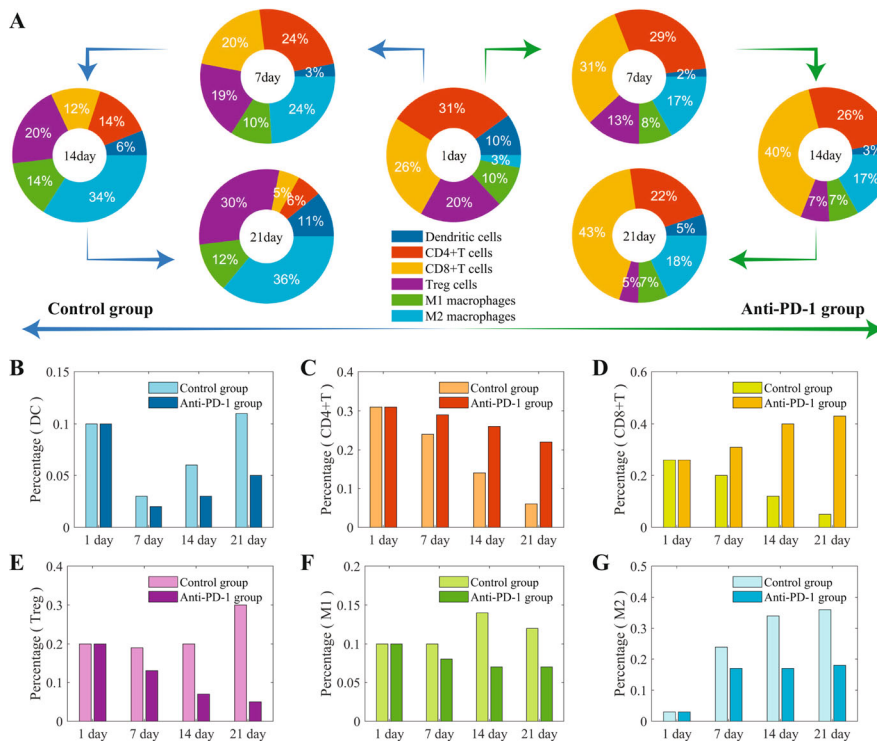


Fig. 7 Evolutionary dynamics in the tumor microenvironment. **A** Percentages of different types of immune cells on days 1, 7, 14, and 21 in the control group (left) and the anti-PD-1 group (right). **B–G** Histograms of the numbers of dendritic cells, CD4⁺T cells, CD8⁺T cells, Treg cells, M1-type macrophages, and M2-type macrophages on days 1, 7, 14, and 21 in the control group and anti-PD-1 group (color figure online)

(−0.909) at the later stage (days 8–21). Consequently, the correlation between tumor cells and dendritic cells transitions from negative (−0.870) to positive (0.9773) as tumor cell numbers increase (Fig. 6B).

Tumor growth is regulated by four key pathways (Fig. 6A): (1) Tumor cells release tumor-associated antigens, which activate dendritic cells. (2) Dendritic cells secrete interleukin 12 to activate the differentiation of naive T cells into effector T cells (T_1 and T_8 cells). (3) The effector T cells then kill the tumor cells. (4) Tumor cells form PD-1-PD-L1 complexes, playing an immunosuppressive role. The immune checkpoint inhibitor (anti-PD-1) blocks the formation of the PD-1-PD-L1 complex (pathway (5)) and suppresses the immunosuppression by tumor cells. At the early stage, there is a negative correlation between tumor cells and effector T cells, indicating weak activation of pathway (1) and immunosuppression of pathway (4). However, pathways (2) and (3) show strong killing effects by effector T cells. As tumor cell numbers increase, pathways (1) and (2) become more active, leading to indirect immune cell activation, while immunosuppressive pathway (4) dominates. Consequently, the correlation between dendritic cells and effector T cells turns negative.

To delve into the dynamics of immune cells during tumor growth and anti-PD-1 treatment, we compared the evolution dynamics for the control and anti-PD-1 groups. Figure 7A illustrates the percentage of immune cells in both groups, with detailed comparisons of each cell type in Fig. 7B–G. The CD4⁺T cell percentage decreased in both control and anti-PD-1 groups, and the decreasing process in the anti-PD-1 group was slower than that in the control group (Fig. 7C). CD8⁺T cell percentages decreased in the control group but increased in the anti-PD-1 group (Fig. 7D). These results indicate the inhibitory role of anti-PD-1 in immune checkpoint regulation. Dendritic cell percentage positively correlated with the tumor cell numbers, the percentage in the anti-PD-1 group was smaller than that in the control group (Fig. 7B). The Treg cell percentage decreased in the control group but increased in the anti-PD-1 group, showing higher values in the anti-PD-1 group (Fig. 7E). Furthermore, the M2-type macrophage percentages were significantly lower in the anti-PD-1 groups compared to the control group (Fig. 7G). Accordingly, the M1-type macrophage percentages showed a higher value in the control group than in the anti-PD-1 group (Fig. 7F).

The observed differences in Treg and M2-type macrophages between the anti-PD-1 and control groups suggest a substantial decrease in tumor microenvironment deterioration during immunotherapy, indicating its potential benefits in restraining tumor progression. Clinically, the abundance of Treg infiltration into tumor tissue is highly correlated with poor clinical prognosis and deterioration of the tumor microenvironment (Tanaka and Sakaguchi 2017). M2-type macrophages play a biological function similar to Treg cells (Lawrence and Natoli 2011; Noy and Pollard 2014). Treg cells and M2-type macrophages are key indicators of the deterioration of the tumor microenvironment.

Model simulations demonstrated that the percentage of Treg cells decreased from 29.45% in the control group to 4.4% in the group treated with a combination of anti-FGFR and anti-PD-1, representing an approximately 85% reduction after the combination treatment. This finding aligns with a recent study that utilized a mathematical model to describe cell and cytokine interactions under treatment with anti-PD-1 and anti-TGF- β (Siewe and Friedman 2021). The study incorporated cancer-specific parameters based on mouse experiments, and it indicated that combination treatment with TGF- β inhibitors and anti-PD-1 led to a roughly 54% reduction in Treg cell levels, dropping 2.90×10^{-3} g/cm³ in the control to 1.35×10^{-3} g/cm³ after combination treatment (Siewe and Friedman 2021). Both studies consistently revealed a reduction in Treg cells following combination therapy. This has inspired us to delve deeper into mathematical models involving different drugs in combination with anti-PD-1 to provide more advantageous drug combination options prior to clinical trials.

3.3 Evaluation of Anti-FGFR and Anti-PD-1 Treatments

There is an evident crosstalk between anti-FGFR and anti-PD-1 treatments. Anti-FGFR inhibits cancer cell proliferation and reduces NEDD4 phosphorylation. The phosphorylation of NEDD4 on the cell surface can lead to the modification of PD-L1 through ubiquitination. Anti-FGFR may cause a high expression of PD-L1, which is formulated by Eq. (15), potentially reducing its inhibitory effects (Jing et al. 2022). The

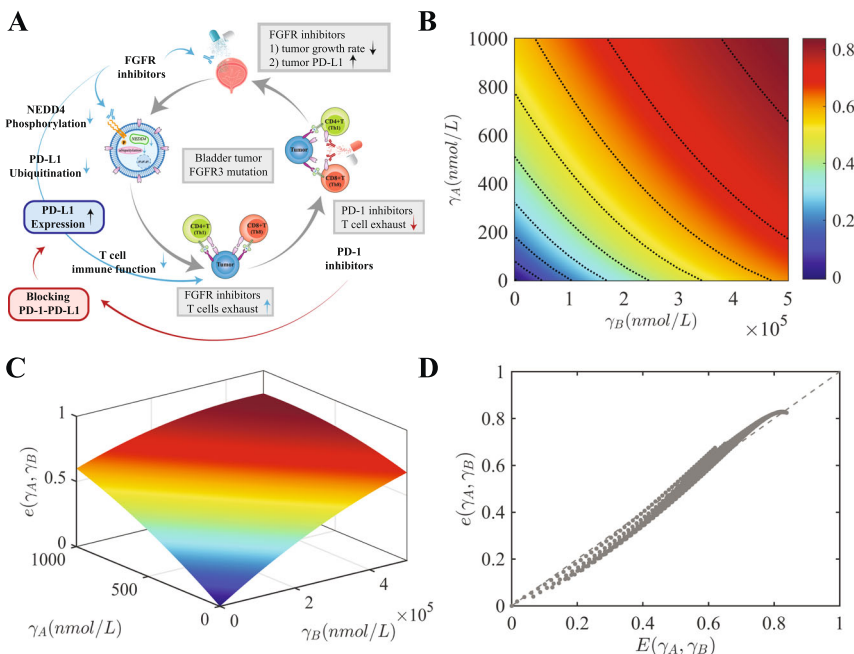


Fig. 8 Analysis of the combination effect of anti-PD-1 (γ_A) and anti-FGFR (γ_B) in treating bladder cancer. **A** Interactions between anti-FGFR and anti-PD-1 treatments in bladder cancer. **B** Combination efficacy map corresponding to different drug combinations (γ_A, γ_B), where the concentration range of γ_A is $0-1 \times 10^5$ nmol/L, and the concentration range of γ_B is $0-5 \times 10^5$ nmol/L. **C** Three-dimensional heat map of the combined efficacy function. **D** Scatter plot of the deviation between numerical solution $E(\gamma_A, \gamma_B)$ and quadratic surface solution $e(\gamma_A, \gamma_B)$ (color figure online)

formation of the PD-1-PD-L1 complex, a target of anti-PD-1 treatment, can counteract the negative effects induced by anti-FGFR. The interactions between these treatments in the context of bladder cancer are summarized in Fig. 8A.

To assess the efficacy of combined anti-PD-1 and anti-FGFR treatment, we explored different drug administration rates (γ_A for anti-PD-1 and γ_B for anti-FGFR) and compared tumor cell numbers at day 21. We defined a combined efficacy function as

$$E(\gamma_A, \gamma_B) = \frac{M_{21}(0, 0) - M_{21}(\gamma_A, \gamma_B)}{M_{21}(0, 0)} \times 100\%, \quad (23)$$

where $M_{21}(\gamma_A, \gamma_B)$ represents the tumor cell number at day 21 with the given administration rates. A larger value of $E(\gamma_A, \gamma_B)$ indicates higher combined efficacy. Simulations revealed a non-linear enhancement of combined efficacy with increasing drug concentrations (Fig. 8B). The simulated combined efficacy can be described through a quadratic function of the form

$$e(\gamma_A, \gamma_B) = a_1\gamma_A + a_2\gamma_B + a_3\gamma_A\gamma_B + a_4\gamma_A^2 + a_5\gamma_B^2, \quad (24)$$

where $a_1 = 1.9 \times 10^{-6}$, $a_2 = 8.1 \times 10^{-4}$, $a_3 = -9.0 \times 10^{-10}$, $a_4 = -1.1 \times 10^{-12}$, $a_5 = -2.1 \times 10^{-7}$. The quadratic function further illustrates the relationship of combination treatment, as depicted in Fig. 8C. We selected 1071 sets of parameters (γ_A, γ_B) and calculated the correspondings values of $E(\gamma_A, \gamma_B)$ and $e(\gamma_A, \gamma_B)$. The comparison between numerical solution $E(\gamma_A, \gamma_B)$ and the quadratic surface solution $e(\gamma_A, \gamma_B)$ is plotted as a scatter plot in Fig. 8D, which shows that the quadratic function $e(\gamma_A, \gamma_B)$ fits well with the numerical result $E(\gamma_A, \gamma_B)$.

Since anti-FGFR increases PD-L1 expression on cancer cell surfaces (Jing et al. 2022), the administration protocol can play a crucial role in tumor growth. We compared three regimens (Fig. 9A): the baseline regimen of the combined group in Fig. 5A, plan 1 by which anti-FGFR followed with combination therapy, and plan 2 by which anti-PD-1 followed with combination therapy. Simulations demonstrated that plan 1 resulted in faster tumor growth than the baseline regimen and plan 2, indicating the importance of the drug administration protocol in suppressing tumor growth (Fig. 9B, C). The baseline regimen exhibited the slowest tumor evolution among the three conditions. These findings underscore the significance of thoughtful drug administration sequencing in optimizing the therapeutic impact.

3.4 Variations in Target Competition Reveal Internal Mechanisms of Tumor Evolution

To explore the impact of drug-receptor binding strength on tumor evolution during immunotherapy, we conducted a parametric analysis of parameters related to target competition. Firstly, we varied the parameters α_1 and α_2 , representing the binding strength of PD-1 to PD-L1 and the anti-PD-1 drug, respectively. The tumor cell numbers increased with α_1 and decreased with α_2 , as illustrated in Fig. 10A. Consequently, the binding of PD-L1 to PD-1 favored tumor growth, and the competitive binding of anti-PD-1 to PD-1 counteracted the inhibition by PD-L1, leading to a deceleration of tumor growth.

To further explore the effect of drug-receptor binding strength on tumor evolution during targeted therapy, we performed parameter analyses on K_1 , K_2 , and K_3 . Notably, K_1 and K_2 denote the activation strength of tumor proliferation via ligand-dependent and ligand-independent pathways, respectively, while K_3 represents the inhibition strength of tumor proliferation by the binding of the targeting drug to the receptor. Varying these parameters over a wide range, the resulting tumor cell numbers at day

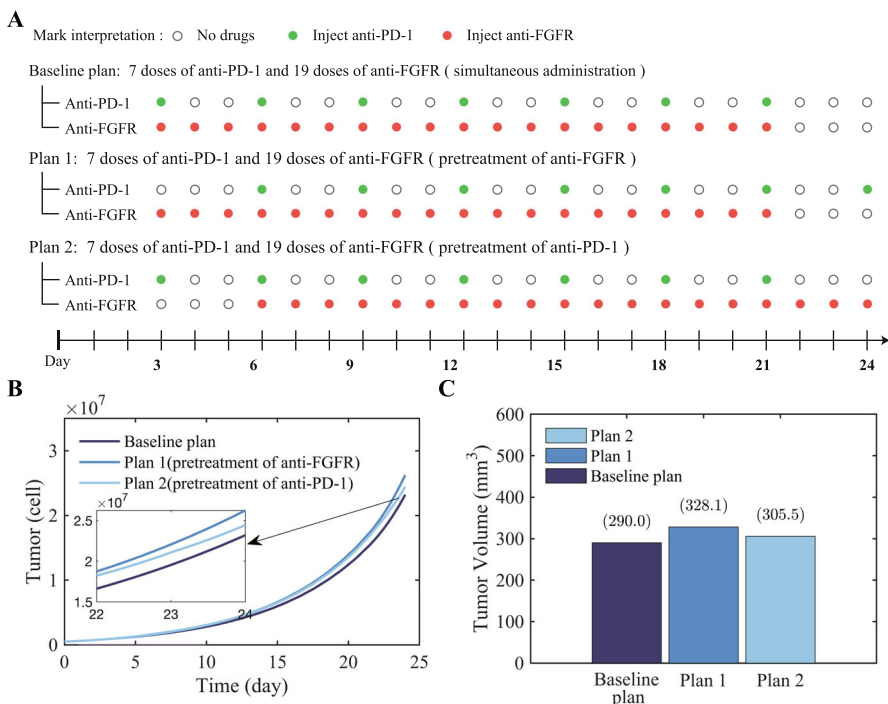


Fig. 9 The impact of administration sequence of anti-PD-1 and anti-FGFR in combination therapy on tumor growth. **A** Schematic of administration of baseline plan, plan 1, and plan 2. **B** Tumor growth under baseline plan, plan 1, and plan 2 treatment strategies. **C** Tumor volume at day 24 under baseline plan, plan 1, and plan 2 treatment strategies (color figure online)

21 are displayed in Fig. 10C. Specifically, when $K_3 = 1.2 \times 10^{-3}$, the tumor cell number increased with the increment of K_2 , representing the dependence of tumor cell number on ligand-independent activated-state receptors (Fig. 10B). However, the tumor cell number exhibited insensitivity to changes in the parameter K_1 (Fig. 10B). Additionally, when $K_1 = 5 \times 10^8$, the tumor cell numbers increased with the increment of K_2 and decreased with the binding strength K_3 (Fig. 10D). These findings suggest that the ligand-independent proliferation mode, represented by the parameter K_2 , is predominant in bladder cancer with FGFR mutations.

To further examine the influence of PD-1 and PD-L1 expression on tumor growth, we performed parameter analyses on the PD-1 production rate ρ_P and the PD-L1 production rate ρ_L . Categorizing the expression rate of PD-1 into high ($\rho_P = 1 \times 10^{-5}$) or low ($\rho_P = 1 \times 10^{-6}$), we observed that high PD-1 expression accelerated tumor cell expansion and inhibited effector T cells, resulting in a low effector T cell number at day 21 (Fig. 11A, B). Conversely, low PD-1 expression maintained a persistent level of effector T cells (Fig. 11B), leading to a smaller number of tumor cells (Fig. 11A).

Varying the PD-L1 expression rate from low ($\rho_L = 1.0 \times 10^{-7}$) to high ($\rho_L = 2.5 \times 10^{-6}$), we evaluated the tumor growth and effector T cell numbers. A low PD-L1 expression rate ($\rho_L = 1.0 \times 10^{-7}$) resulted in potential tumor obliteration after initial

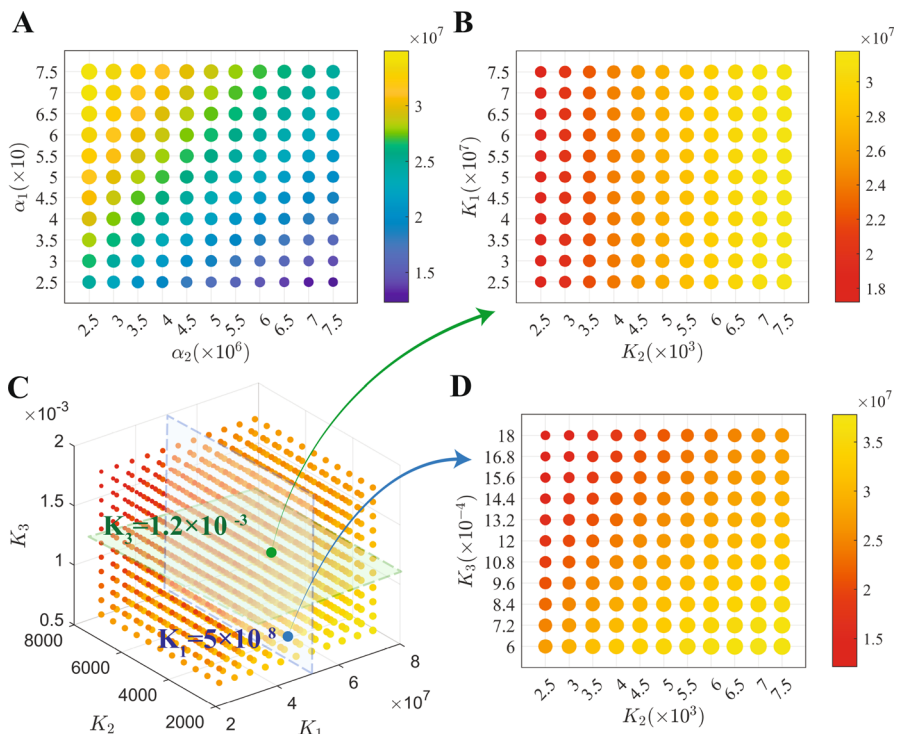


Fig. 10 Parametric analysis of target competition model. **A** Dependence of tumor size with parameters α_1 and α_2 in target competition model of anti-PD-1. **B** Dependence of tumor size with K_1 and K_2 in target competition model of anti-FGFR. **C** Dependence of tumor size with K_1 , K_2 , and K_3 in target competition model of anti-FGFR. The color and size of points in the scatter diagram depict the tumor size at day 21 following the anti-PD-1 group or anti-FGFR group in Fig. 5A (color figure online)

tumor growth, while a higher PD-L1 expression rate led to uncontrolled expansion, as depicted in Fig. 11C. Correspondingly, higher levels of PD-L1 inhibited effector T cells through a factor $F(P, L)$ defined by Eq. (17). Increased PD-L1 expression can strengthen the inhibition of T cell activation, resulting in a lower number of effector T cells (Fig. 11D). These results highlight the profound impact of immune checkpoints on tumor and T cell evolutions during immunotherapy, with changes in PD-L1 expression significantly influencing effector T cells and tumor growth.

3.5 Disease Progression Revealed by Virtual Experiment Technology

To gain a better understanding of cancer evolution through the proposed mathematical model, we conducted virtual experiments. Virtual experiment technology involves combining a mathematical model with a machine learning algorithm to produce and analyze virtual data that displays tumor progression under different conditions (Kozłowska et al. 2020). This innovative technology is particularly valuable for can-

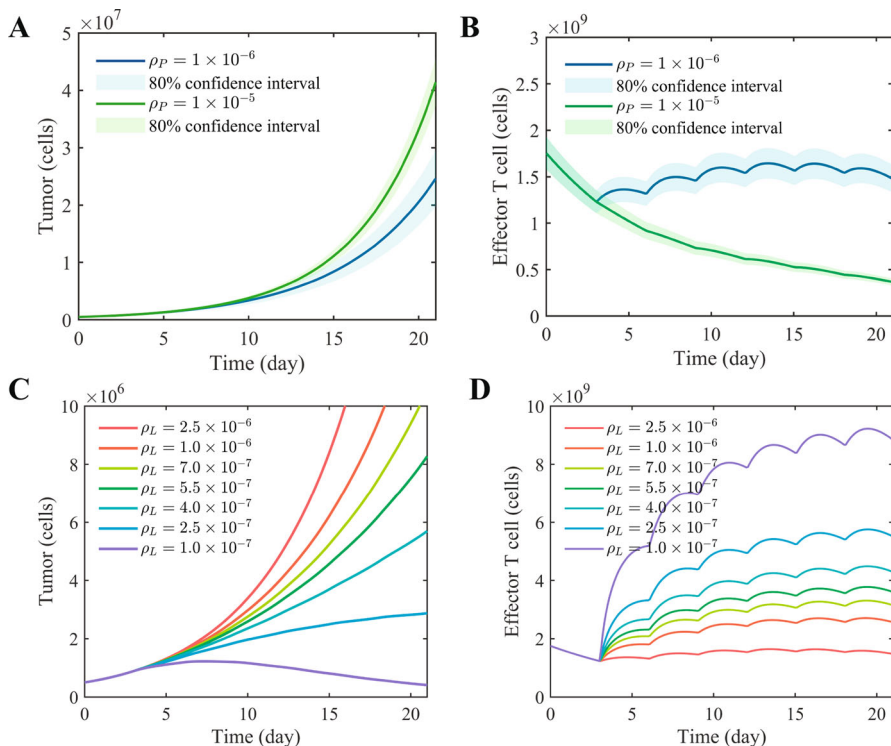


Fig. 11 Effects of different expression rates of immune checkpoints in tumor growth and effector T cells number. **A** Evolution of tumor cells with different PD-1 expression rates. **B** Evolution of effector T cells with different PD-1 expression rates. **C** Evolution of tumor cells with different PD-L1 expression rates. **D** Evolution of effector T cells with different PD-L1 expression rates. Results show the evolution dynamics following the anti-PD-1 group in Fig. 5A (color figure online)

cer progression research when real experimental or clinical data is scarce (Kozłowska et al. 2020; Ma et al. 2023). Our study calibrated the mathematical model using experimental data on bladder cancer. We utilized the random sampling method to sample model parameters and generate a set of virtual experiments.

We conducted a sensitivity analysis following the proposed model to identify crucial parameters for generating virtual experiments. Representing the number of tumor cells at day 21 with a given parameter set $X^0 = (x_1^0, x_2^0, \dots, x_n^0)$ as $V(X^0)$, we defined the local sensitivity concerning the i 'th parameter as:

$$S_i(X^0) = \frac{V(x_1^0, \dots, x_i^0 + \delta x_i, \dots, x_n^0) - V(X^0)}{V(X^0)}, \quad (i = 1, \dots, n) \quad (25)$$

where δx_i denotes the variation in the i 'th parameter. Positive (or negative) values of $S_i(X^0)$ indicated positive (or negative) correlations between the quantized output V and the parameter x_i . Pertinent parameters related to drug effects on tumor cell evolu-

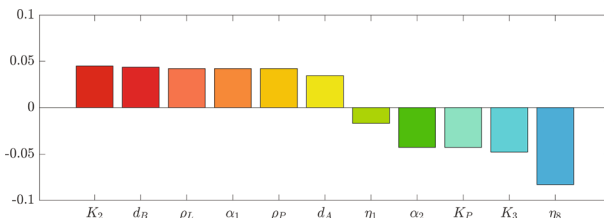


Fig. 12 Results of parametric sensitivity analysis (color figure online)

tion, including ρ_P , ρ_L , α_1 , α_2 , K_P , d_A , K_2 , K_3 , d_B , η_1 , and η_8 , were predominantly considered.

Results from the sensitivity analysis are depicted in Fig. 12. Notably, expression rates of immune checkpoints, ρ_P and ρ_L , exhibited positive correlations to tumor growth, while the immune checkpoint inhibition constant K_P showcased a negative correlation. Among drug-related parameters, drug consumption rates d_A and d_B positively correlated with tumor growth, whereas drug binding strengths α_2 and K_3 displayed negative correlations. Furthermore, immunosuppressive pathway parameters α_1 and K_2 of the tumor cells positively correlated with tumor growth during progression. Conversely, tumor-killing rates η_1 and η_8 by the immune cells exhibited negative correlates.

For the implementation of virtual experiments, parameters related to the background bladder cancer (θ_C and d_C), expressions of target proteins (ρ_P , ρ_L , and ρ_B), competition of tumor targets (K_1 , K_2 , and K_3), and competition of immune checkpoints (α_1 and α_2) were considered. Parameters were sampled using the random sampling method within a fluctuation range from $\pm 10\%$ to $\pm 100\%$ (Fig. 13A), with each parameter set representing a virtual mouse. Numerical solutions were obtained for the model equation based on the four protocols of control, anti-PD-1, anti-FGFR, and combined treatment in Fig. 5A. The numerical scheme of virtual experiment technology is illustrated in Fig. 13A.

Survival analysis was performed using virtual experimental data, with a virtual mouse considered death when the tumor cell number exceeded a threshold of 2×10^8 cells. The survival function was then calculated using Kaplan-Meier survival analysis:

$$S(t) = \frac{\text{No. survival mice}}{\text{No. total mice}} \times 100\%. \quad (26)$$

The survival functions for the four virtual groups are presented in Fig. 13B–F. Notably, the combination treatment significantly improved the probability of survival, with anti-PD-1 immunotherapy proving to be more effective than targeted therapy based on anti-FGFR.

The tumor cell numbers in survival virtual mice at day 21 were analyzed to measure tumor load using the kernel density function. Figure 13G shows the resulting density function obtained from 500 virtual mice in each. The combination treatment regimen notably reduced tumor growth compared to the control group. Additionally, anti-PD-1 treatment resulted in a smaller distribution of tumor cell numbers compared to anti-FGFR treatment.

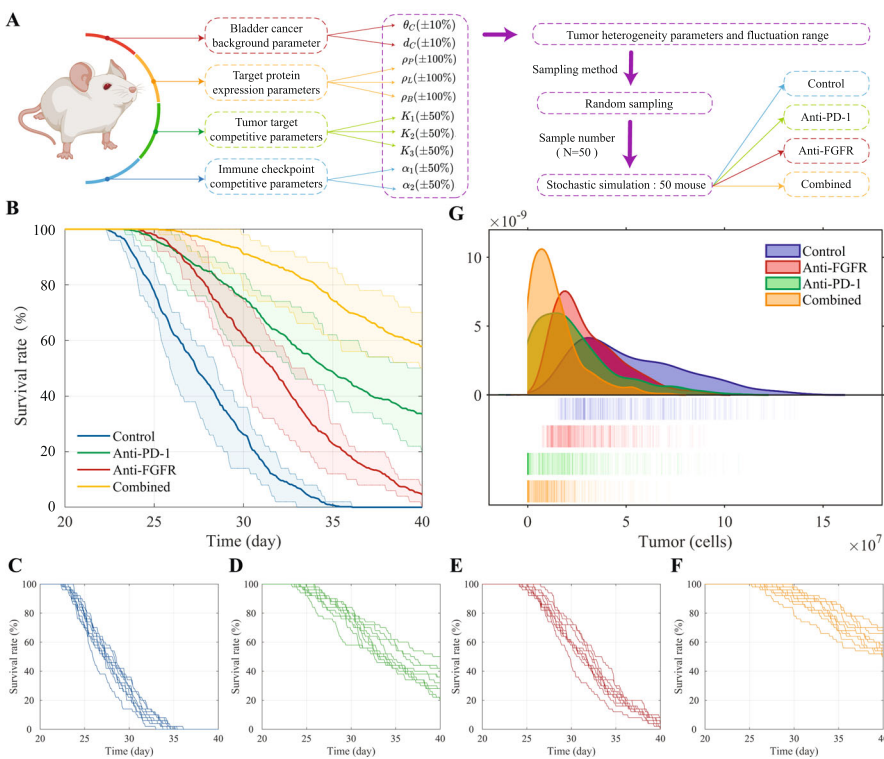


Fig. 13 Virtual experiment technology and survival analysis. **A** The methodology for sampling tumor heterogeneity and the computational framework underlying the virtual experiment technology. **B** Survival analysis results of mice subjected to various treatment regimens. Solid lines represent the mean effects derived from stochastic simulations, while the shaded areas indicate the confidence interval generated throughout these stochastic simulations. **C–F** Survival analysis of 10 stochastic simulations (50 mice per randomized trial) in the control group (**C**), anti-PD-1 group (**D**), anti-FGFR group (**E**), and combination therapy group (**F**). **G** Distribution of tumor cell nuclear density in mice under different treatment regimens (color figure online)

To further analyze the progression of the disease, virtual mice were divided into four stages based on tumor cell numbers: stage I ($C < 5 \times 10^7$), stage II ($5 \times 10^7 < C < 1 \times 10^8$), stage III ($1 \times 10^8 < C < 2 \times 10^8$), and stage IV ($C > 2 \times 10^8$). The chord diagrams in Fig. 14 show the tumor progression for the four groups of virtual mice.

On day 10, most control mice, nearly all mice treated with anti-PD-1 or anti-FGFR, and all mice treated with the combination of drugs remained in stage I. A small number of control mice and mice treated with individual drugs progressed to stage II. The efficacy of immunotherapy and targeted therapy was similar on day 10 (Fig. 14A).

On day 20, all control mice had progressed to stage II or III, all mice treated with anti-FGFR, and most mice treated with anti-PD-1 progressed to stage II. A small number of anti-PD-1 treated mice remained at stage I. Mice treated with combination drugs either progressed to stage II or remained at stage I (Fig. 14B).

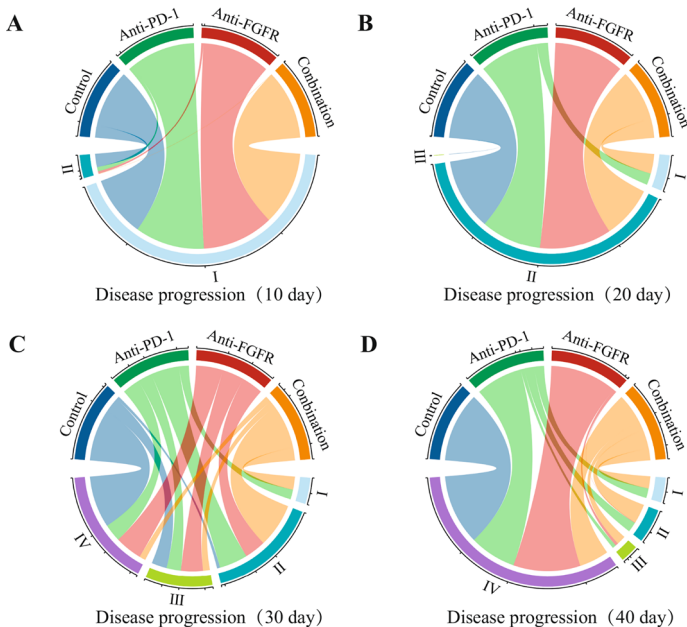


Fig. 14 Disease progression of virtual mice on day 10 (A), day 20 (B), day 30 (C), and day 40 (D). The upper part of the chord diagram represents the experimental groups, and the lower part represents the four stages of tumor progression (color figure online)

On day 30, the majority of control mice had progressed to stage IV, mice treated with targeted therapy had a distribution of stages II through IV, and a small proportion of mice treated with anti-PD-1 or combination drugs remained in stage I (Fig. 14C).

On day 40, control mice and nearly all mice receiving targeted therapy had advanced to stage IV. Mice receiving immunotherapy and combination therapy had advanced to all four stages of the disease (Fig. 14D). At day 40, the mice treated with anti-PD-1 or combination drugs showed slower tumor progression compared to other groups (Fig. 14D), suggesting that immunotherapy treatment (anti-PD-1) was more effective than target treatment (anti-FGFR) in preventing bladder cancer progression with FGFR mutation.

4 Discussion

Bladder cancer is the most common malignant tumor in the urinary system and presents a significant global health challenge (Patel et al. 2020; Lenis et al. 2020). An abnormal expression of FGFR, a prominent characteristic of bladder cancer, leads to excessive activation of intracellular signaling pathways, promoting cancer cell proliferation and survival (Katoh 2019; Babina and Turner 2017). This indicates that targeting therapy directed at FGFR may have the potential to benefit patients with advanced bladder cancer (Katoh 2019; Babina and Turner 2017). However, the recurrence of tumors after FGFR inhibitor treatment has posed a significant challenge in clinical treatment. Addi-

tionally, while FGFR-targeted therapy shows remarkable efficacy in specific patient populations, the development of resistance mechanisms and disease recurrence highlights the need for complementary strategies (Katoh 2019; Babina and Turner 2017; Maeng et al. 2010; Tomlinson et al. 2007).

Immunotherapy, especially immune checkpoint inhibitors like PD-1 blockade, has had a significant impact on cancer treatment (Topalian et al. 2012; Postow et al. 2015). These inhibitors are now widely used to treat bladder cancer, with some approved and recommended as standard treatments. However, due to varying responses to treatment, drug resistance, and severe side effects in patients, the clinical benefits of using these drugs alone are limited (Topalian et al. 2012; Davar and Kirkwood 2019). Therefore, it is important to find ways to improve the clinical benefits of immunotherapy and reduce the risk of tumor recurrence.

Recently, there has been growing interest in combining targeted therapy with immunotherapy to improve cancer treatment (Hughes et al. 2016; Bergholz et al. 2020; Colli et al. 2017). This approach aims to maximize the benefits of both methods while addressing their individual limitations. We have developed a mathematical model for combination therapy using the latest experimental data on FGFR inhibitors and PD-1 inhibitors. This model explores how immune checkpoint inhibitors work by constructing a regulatory network of the tumor microenvironment. Additionally, we have developed a novel tumor evolution dynamics model based on the competitive binding of drugs, ligands, and receptors, which integrates their roles in cell proliferation. Our focus on combining FGFR3-targeted therapy with PD-1 immunotherapy aligns with current efforts to improve treatment effectiveness and expand the number of patients who can benefit from it.

The current study utilized virtual experiments driven by mathematical modeling and machine learning to make predictions based on model simulations. By creating a virtual group of experimental mice, this technology provides a powerful tool for predicting treatment outcomes and exploring scenarios that might be challenging to investigate solely through traditional experimental methods (Cappuccio et al. 2016; Arulraj et al. 2024). The sensitivity analysis conducted in this study provides insights into key parameters that influence tumor evolution and treatment response. Identifying parameters such as immune checkpoint expression rates, drug consumption rates, and drug binding strengths adds granularity to our understanding of the complexities. Being able to pinpoint these influential factors is crucial for refining treatment strategies and potentially guiding personalized therapeutic approaches.

The study results indicate that using a combination of therapies leads to a significant decrease in tumor size. When the body is unable to tolerate both drugs simultaneously, starting with anti-PD-1 treatment followed by anti-FGFR treatment proves to be more effective. We have also found that receptors on the surface of tumor cells, which are activated independently of ligands, are primarily responsible for tumor growth. FGFR inhibitors can effectively halt the signaling that promotes tumor cell growth, thereby reducing their proliferation. Additionally, the rate at which PD-L1 is expressed plays a crucial role in how tumor and immune cells evolve over time, and PD-L1 inhibitors may have a greater impact compared to PD-1 inhibitors.

Despite successfully predicting tumor growth, the current mathematical model has limitations that need to be addressed. We recognize that the established mathemat-

ical model has not considered the following key aspects: (1) the important role of angiogenesis in tumor immunology; (2) pharmacokinetics and pharmacodynamics; (3) multi-compartment modeling of tumor immunology (Arulraj et al. 2024; Wang et al. 2023; Cappuccio et al. 2016). Future versions of the model could benefit from integrating insights obtained from research on tumor microenvironment dynamics, spatial heterogeneity, and the immune system's impact on treatment responses (Arulraj et al. 2024; Wang et al. 2023; Cappuccio et al. 2016; Lai et al. 2018; Dagogo-Jack and Shaw 2018).

In addition, new types of treatments like adoptive cell therapies and cancer vaccines add more complexity to the way we treat cancer (Santana-Davila et al. 2017). It would be valuable to study how these treatments work together with existing FGFR-targeted and immunotherapeutic approaches. The mathematical framework developed in this study forms a strong basis for incorporating these complexities and broadening our knowledge of combination therapies in cancer treatment.

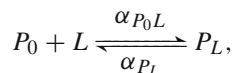
In conclusion, combining mathematical modeling, machine learning, and virtual experiments offers a valuable approach to understanding the complexities of combination therapies (Kozłowska et al. 2020; Arulraj et al. 2024). As the scientific community continues to uncover the details of cancer biology and therapeutic interventions, multidisciplinary studies like the one presented here contribute to our overall knowledge. The findings and methodologies introduced in this study provide a strong foundation for future investigations aiming to optimize combination strategies and advance the field of cancer therapeutics.

Appendix A Mathematical Formulations

A.1 Target Competition Model: Anti-PD-1

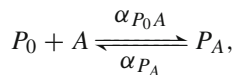
In the model of competition among immune checkpoint inhibitors, anti-PD-1 competes with PD-L1 to bind with PD-1. PD-1, found on the surface of T cells, can bind to either anti-PD-1 or PD-L1 on the surface of tumor cells. When the PD-1-PD-L1 complex forms, it allows tumor cells to exert immunosuppressive effects. On the other hand, the formation of the PD-1-anti-PD-1 complex dilutes the PD-1 sites on the T cell surface, thereby preventing the immunosuppressive effects from the tumor cells. In our study, we established the formulation of PD-1-PD-L1 complexes in the presence of anti-PD-1 using chemical rate equations and the law of mass conservation, based on the receptor's capacity to bind to drugs or ligands.

PD-L1 binds to free PD-1 on the T cell surface, mediating immunosuppression through the chemical reaction:



where P_0 represents the free-state PD-1 on the cell surface, L represents the PD-L1 on the cell surface, P_L represents the PD-1-PD-L1 complex, α_{P_0L} is the binding rate of P_0 to L , and α_{P_L} is the dissociation rate of P_L .

Anti-PD-1 binds to the free-state PD-1 on the T cell surface to form a PD-1-anti-PD-1 complex, diluting the proportion of free-state PD-1 on the T cell surface to avoid immunosuppressive effects. The chemical reaction process is shown as:



where A stands for the immune checkpoint inhibitor anti-PD-1, P_A stands for the anti-PD-1-PD-1 complex, α_{P_0A} is the binding rate of P_0 to A , and α_{P_A} is the dissociation rate of P_A .

The chemical rate equations for the above two reactions are given by:

$$\begin{aligned}\frac{dP_L}{dt} &= \alpha_{P_0L} P_0 L - \alpha_{P_L} P_L, \\ \frac{dP_A}{dt} &= \alpha_{P_0A} P_0 A - \alpha_{P_A} P_A.\end{aligned}$$

Since the binding and dissociation of proteins are fast processes compared to changes in the cell numbers, we applied the quasi-steady-state assumption to derive the specific expression forms of the PD-1-PD-L1 complex and the PD-1-anti-PD-1 complex:

$$\begin{aligned}P_L &= \frac{\alpha_{P_0L}}{\alpha_{P_L}} P_0 L = \alpha_1 P_0 L, \\ P_A &= \frac{\alpha_{P_0A}}{\alpha_{P_A}} P_0 A = \alpha_2 P_0 A,\end{aligned}$$

where $\alpha_1 = \frac{\alpha_{P_0L}}{\alpha_{P_L}}$ is the equilibrium constant for the binding process of P_0 to L , and $\alpha_2 = \frac{\alpha_{P_0A}}{\alpha_{P_A}}$ is the equilibrium constant for the binding process of P_0 to A .

The total concentration of PD-1 is expressed as a sum of different state PD-1 proteins:

$$P = P_0 + P_L + P_A.$$

Substituting the expressions for P_L and P_A , we have

$$P = P_0 + \alpha_1 P_0 L + \alpha_2 P_0 A.$$

Thus,

$$P_0 = \frac{P}{1 + \alpha_1 L + \alpha_2 A},$$

and

$$P_L = \frac{\alpha_1 L P}{1 + \alpha_1 L + \alpha_2 A},$$

$$P_A = \frac{\alpha_2 A P}{1 + \alpha_1 L + \alpha_2 A}.$$

Here, P_L represents the PD-1-PD-L1 concentration in the case of competition between anti-PD-1 and PD-L1. Thus, the immune checkpoint inhibitory function F in (2) and (3) is expressed as:

$$F(P, L, A) = \frac{1}{1 + P_L/K_P}, \text{ where } P_L = \frac{\alpha_1 L P}{1 + \alpha_1 L + \alpha_2 A},$$

where K_P is the immune checkpoint inhibitory constant.

A.2 Target Competition Model: Anti-FGFR

The mutated free-state receptor (R_0) on the tumor cell surface can convert into an activated-state receptor (R_1^*) in a ligand-dependent form, or into an activated-state receptor (R_2^*) in a ligand-independent form. These activated-state receptors trigger downstream pathways that mediate tumor proliferation. Additionally, the targeted inhibitor anti-FGFR (B) can specifically bind to the mutated free-state receptors on the tumor cell surface, forming a drug-binding receptor (\bar{R}). This reduces the concentration of mutated free-state receptors, diminishing the proportion of activated receptors, and ultimately impacting tumor cell proliferation. In essence, activating mutations in FGFR on bladder cancer cell surfaces have dual effects: enhancing ligand-receptor binding strength to expedite tumor proliferation signaling, and activating downstream signaling pathways through a non-ligand-dependent route to regulate tumor proliferation. Here, we categorize the three ways FGFR mediates tumor proliferation on the surface of bladder cancer cells.

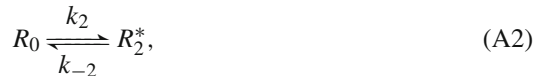
The mutant free-state receptor (R_0) binds to a ligand (L_r) to form a ligand-dependent activated-state receptor (R_1^*), initiating downstream signaling pathways and facilitating tumor growth. Tumor cells interact with environmental ligands through receptors on their cell membranes, triggering signaling pathways within the tumor cell and promoting cell proliferation. Mutations in the tumor cell receptor increase the receptor's binding affinity for the ligand. The chemical reaction can be presented as:



where L_r represents the ligand binding to the mutated free-state receptor R_0 , R_1^* represents the ligand-dependent activated-state receptor, k_1 denotes the binding rate of the receptor to the ligand, and k_{-1} denotes the dissociation rate of the ligand-receptor complex.

The mutant free-state receptor (R_0) is capable of forming an activated-state receptor (R_2^*) without relying on the presence of the ligand (L_r). This reaction can be

represented as follows:



where R_2^* represents the ligand-independent activated-state receptor, while k_2 and k_{-2} are transition rates between different activation states of the receptor. The ligand-independent activation of the receptor can be likened to the specific process of intracellular phosphorylation and dephosphorylation of the kinase. The activated-state receptors play a role in activating downstream signaling pathways, which in turn mediate tumor proliferation. This is a significant factor in the transition of cancer cells from a dormant state to a proliferation state.

The mutant free-state receptor (R_0) can also bind to FGFR inhibitor (B), thereby blocking downstream signaling pathways and repressing tumor growth. The chemical reaction is described as:



where B represents the targeted drug, \bar{R} represents the drug-binding receptor (i.e., the drug-receptor complex), k_3 is the binding rate of the drug to the receptor, and k_{-3} is the dissociation rate of the drug-receptor complex. The tyrosine kinase inhibitor binds to and reduces the enzymatic activity of FGFR, inhibiting FGFR phosphorylation and related signaling pathways. In our model, we assumed that the targeting agent binds to the mutant free-state receptors, reducing the ratio of free receptors on the cell surface and thus slowing down tumor growth.

The proliferation rate of a tumor cell is determined by the fraction of activated receptors on the cell surface. Now, we derive the proliferation rate based on the above reactions.

From the reactions (A1)–(A3), the equations for R_1^* , R_2^* , and \bar{R} are given by chemical rate equations as:

$$\begin{aligned} \frac{dR_1^*}{dt} &= k_1 L_r R_0 - k_{-1} R_1^*, \\ \frac{dR_2^*}{dt} &= k_2 R_0 - k_{-2} R_2^*, \\ \frac{d\bar{R}}{dt} &= k_3 R_0 B - k_{-3} \bar{R}. \end{aligned}$$

Since protein interactions are fast time-scale processes, we applied the quasi-steady-state assumption to derive concentrations of different state receptors as follows:

$$R_1^* = \frac{k_1 L_r}{k_{-1}} R_0, \quad R_2^* = \frac{k_2}{k_{-2}} R_0, \quad \bar{R} = \frac{k_3 B}{k_{-3}} R_0.$$

The concentration of total activated-state receptors is further expressed as:

$$R^* = R_1^* + R_2^* = \left(\frac{k_1 L_r}{k_{-1}} + \frac{k_2}{k_{-2}} \right) R_0.$$

Thus, we obtain the relations between R_0 , \bar{R} , and R^* as:

$$R_0 = \frac{1}{k_1 L_r / k_{-1} + k_2 / k_{-2}} R^*, \quad (\text{A4})$$

and

$$\bar{R} = \frac{k_3}{k_{-3}} \times \frac{B}{k_1 L_r / k_{-1} + k_2 / k_{-2}} R^*. \quad (\text{A5})$$

According to the law of mass conservation, the total concentration R of cell surface receptors can be expressed as

$$R = R_0 + R^* + \bar{R}, \text{ where } R^* = R_1^* + R_2^*. \quad (\text{A6})$$

Substituting (A4)–(A5) into (A6), we obtain

$$R = R^* + \left(\frac{1}{k_1 L_r / k_{-1} + k_2 / k_{-2}} \right) R^* + \frac{k_3}{k_{-3}} B \left(\frac{1}{k_1 L_r / k_{-1} + k_2 / k_{-2}} \right) R^*.$$

Let $\tilde{K}_1 = \frac{k_1}{k_{-1}}$ denoting the equilibrium constant of the ligand-dependent activation process, $K_2 = \frac{k_2}{k_{-2}}$ denoting the equilibrium constant of ligand-independent activation process, and $K_3 = \frac{k_3}{k_{-3}}$ denoting the equilibrium constant of the receptor-drug complex, we have the fraction of activated receptors:

$$\frac{R^*}{R} = \frac{\tilde{K}_1 L_r + K_2}{1 + \tilde{K}_1 L_r + K_2 + K_3 B}. \quad (\text{A7})$$

The equation for the change in ligand FGF (L_r) is given by:

$$\frac{dL_r}{dt} = \lambda - \mu_{Lr} C L_r,$$

where λ represents the production rate of FGF and μ_{Lr} is the binding rate of ligand to tumor cells. Applying the quasi-steady-state assumption, we obtain

$$L_r = \frac{\lambda}{\mu_{Lr} C}.$$

Finally, substituting L_r into Eq. (A7) and let $K_1 = \frac{\tilde{K}_1 \lambda}{\mu_{Lr}}$, the activated-state receptor ratio R^*/R is given by:

$$\frac{R^*}{R} = \frac{K_1 + K_2 C}{C + K_1 + K_2 C + K_3 B C}.$$

Here, K_1 represents the equilibrium constant for the ligand binding process.

The proliferation rate of tumor cells is proportional to the ratio R^*/R . Thus, let $\tau(C) = K_1 + K_2C$, the proliferation rate (20) is expressed as:

$$\lambda(C, B) = \theta_C \times \frac{R^*}{R} = \frac{\theta_C \times \tau(C)}{C + \tau(C) + \varphi(B, C)}, \quad (\text{A8})$$

where θ_C is the maximum proliferation rate of tumor cells. Additionally, in the absence of drug action, i.e., the drug action term $\varphi(B, C) = K_3BC = 0$, the proliferation rate is expressed in the form of Michaelis-Menten function:

$$\lambda(C) = \theta_C \times \frac{R^*}{R} = \theta_C \times \frac{\tau(C)}{C + \tau(C)}. \quad (\text{A9})$$

Equations (A8) and (A9) give the proliferation rate of tumor cells with and without anti-FGFR drug.

Appendix B Conversation of Experimental Data

We referred to the experimental results from different sources to perform parameter estimations following experimental data. Since different sources may have different units for the quantities, we need to unify the values by converting different units.

B.1 Drug Concentration Conversion

The unit mg/kg is commonly used for measuring drug doses in clinical practice. In our study, we converted drug units from mg/kg to nmol/L using the drug concentration conversion equation presented in Okuneye et al. (2021):

$$c(\text{nmol/L}) = \chi \times \frac{m(\text{g})}{V(\text{L}) \times M_{\text{mol}}(\text{g/mol})} \times 10^9. \quad (\text{B10})$$

Here, $c(\text{nmol/L})$ represents the concentration in unit nmol/L, $m(\text{g})$ is the mass of drug administered per mouse in grams, $V(L)$ is the volume of a mouse in liters, $M_{\text{mol}}(\text{g/mol})$ is the molar mass of the drug, and χ is the equivalent conversion factor for mouse experiments, often used in medical research to apply the body surface area conversion method. In our study, we used $\chi = 9.1$, $V = 2 \times 10^{-2}$ L.

The standard amount of drug administration is usually measured in mg/kg, and for a mouse weighing about 20 mg = 0.02 kg, the unit of drug administration per mouse is 0.02 mg = 2×10^{-5} g.

For instance, the molecular formula of the PD-1 inhibitor (Nivolumab) is $C_{6362}H_{9862}N_{1712}O_{1995}S_{42}$, which allowed us to convert an experimental dose of 10 mg/kg to 6.5×10^2 nmol/L. Similarly, an FGFR inhibitor (Erdafitinib) with molecular formula $C_{25}H_{30}N_6O_2$ was used to convert an experimental dose of 12.5 mg/kg to 2.5×10^5 nmol/L.

Table 3 Initial value selection

Variate	Value used	References
C	5.00×10^5	Jing et al. (2022)
D	3.10×10^8	Chen and Lai (2022)
T_1	9.50×10^8	Estimation
T_8	8.04×10^8	Chen and Lai (2022)
T_r	6.21×10^8	Chen and Lai (2022)
M_1	3.00×10^8	Estimation
M_2	1.00×10^8	Estimation

B.2 The Transformation Between Cell Number, Volume, and Mass

In our study, we obtained the number of tumor cells by solving the ODE model. We then converted the cell number into tumor volume using the formula

$$V = \frac{C}{\rho}, \quad (\text{B11})$$

where V represents the tumor cell volume (unit: mm^3), C is tumor cell number (unit: cells), and ρ is the tumor cell density (unit: cells/ mm^3). In our calculations, we used $\rho = 8 \times 10^4$ cells/ mm^3 .

To compare our simulated results with the mass data M (unit: g) obtained from experiments, we converted the mass into tumor volume using the formula

$$V = \frac{M}{\rho_M} \quad (\text{B12})$$

where ρ_M represents the density in tumor mass. Since tumor tissues are slightly denser than normal tissues, we assumed the density of the tumor as $\rho_M = 1.1 \times 10^{-3}$ g/ mm^3 .

Appendix C Initial Values and Parameters

The initial cell numbers used in model simulations are listed in Table 3.

The parameters for the immune cell equations are listed in Table 4.

The parameters for the cytokine equations are listed in Table 5.

Acknowledgements This work was funded by the National Natural Science Foundation of China (NSFC 12331018).

References

- Acevedo VD, Ittmann M, Spencer DM (2009) Paths of FGFR-driven tumorigenesis. *Cell Cycle* 8(4):580–588. <https://doi.org/10.4161/cc.8.4.7657>

Table 4 Description of related parameters of immune cell equation

Notation	Description	Value used	Units	References
D_0	The number of naive DCs	1.94×10^7	cells	Chen and Lai (2022)
T_{10}	The number of naive CD4 ⁺ T cells	1.88×10^9	cells	Chen and Lai (2022)
T_{80}	The number of naive CD8 ⁺ T cells	9.39×10^8	cells	Chen and Lai (2022)
M	The number of monocytes	8.00×10^7	cells	Estimation
λ_{DC}	Activation rate of DCs by tumor cells	20.00	day ⁻¹	Chen and Lai (2022)
$\lambda_{T_1 I_{12}}$	Activation rate of CD4 ⁺ T cells by IL-12	27.96	day ⁻¹	Lai et al. (2018)
$\lambda_{T_8 I_{12}}$	Activation rate of CD8 ⁺ T cells by IL-12	24.90	day ⁻¹	Lai et al. (2018)
$\lambda_{T_1 I_2}$	Appreciation rate of CD4 ⁺ T cells by IL-2	25.00	day ⁻¹	Estimation
$\lambda_{T_8 I_2}$	Appreciation rate of CD8 ⁺ T cells by IL-2	75.00	day ⁻¹	Estimation
$\lambda_{T_r T_\beta}$	Activation rate of Treg by TGF- β	1.50	day ⁻¹	Estimation
$\lambda_{M I_\gamma}$	Polarizability of monocytes by IFN- γ	1.00	day ⁻¹	Estimation
$\lambda_{M I_{10}}$	Polarizability of monocytes by IL-10	1.50	day ⁻¹	Estimation
β_1	Phenotype change rate of M1 to M2 macrophages	0.15	day ⁻¹	Lai et al. (2018)
β_2	Phenotype change rate of M2 to M1 macrophages	2.34×10^{-3}	day ⁻¹	Lai et al. (2018)
d_D	Death rate of DCs	0.30	day ⁻¹	Li et al. (2022)
d_{T_1}	Death rate of CD4 ⁺ T cells	0.10	day ⁻¹	Estimation
d_{T_8}	Death rate of CD8 ⁺ T cells	0.10	day ⁻¹	Estimation
d_{T_r}	Death rate of Tregs	0.10	day ⁻¹	Estimation

Table 4 continued

Notation	Description	Value used	Units	References
d_{M_1}	Death rate of M1	0.30	day ⁻¹	Li et al. (2022)
d_{M_2}	Death rate of M2	0.30	day ⁻¹	Li et al. (2022)
K_C	Half-saturation of tumor cells	1×10^7	cells	Estimation
K_{I_2}	Half-saturation of IL-2	2.37×10^{-2}	ng mL ⁻¹	Lai and Friedman (2017a)
$K_{I_{12}}$	Half-saturation of IL-12	8.00×10^{-1}	ng mL ⁻¹	Lai and Friedman (2017a)
$K_{I_{10}}$	Half-saturation of IL-10	8.75×10^{-2}	ng mL ⁻¹	Lai and Friedman (2017a)
$K_{T\beta}$	Half-saturation of TGF- β	2.06×10^{-1}	ng mL ⁻¹	Lai and Friedman (2017a)
$K_{I\gamma}$	Half-saturation of IFN- γ	1.80×10^{-2}	ng mL ⁻¹	Li et al. (2022)
$K_{T\alpha}$	Half-saturation of TNF- α	3.00×10^{-2}	ng mL ⁻¹	Lai et al. (2018)
K_{M_c}	Half-saturation of M-CSF	1.00	ng mL ⁻¹	Lai et al. (2018)
θ_C	Maximum growth rate of tumor cells	0.342	day ⁻¹	Estimation
d_C	Death rate of tumor cells	0.142	day ⁻¹	Estimation
η_1	Killing rate of tumor cells by CD4 ⁺ T cells	1.00×10^{-11}	cells ⁻¹ day ⁻¹	Estimation
η_8	Killing rate of tumor cells by CD8 ⁺ T cells	4.00×10^{-11}	cells ⁻¹ day ⁻¹	Estimation
ρ_P	Expression rate of PD-1 in T cell	1.00×10^{-6}	nmol L ⁻¹ cell ⁻¹	Estimation
ρ_L	Expression rate of PD-L1 in T cell	2.50×10^{-6}	nmol L ⁻¹ cell ⁻¹	Estimation
ρ_B	Expression rate of PD-L1 by FGFR inhibitor	1.00×10^{-6}	nmol L ⁻¹ cell ⁻¹	Estimation

Table 4 continued

Notation	Description	Value used	Units	References
ε_C	Amplification coefficient of PD-L1 in tumor cells	50.00	–	Storey et al. (2020)
α_1	Equilibrium constant for the PD-1-PD-L1 process	50.00	$L \text{ nmol}^{-1}$	Estimation
α_2	Equilibrium constant for the PD-1-anti-PD-1 process	5.00×10^6	$L \text{ nmol}^{-1}$	Estimation
K_P	Immune checkpoint inhibition constant	2.00×10^{-4}	nmol L^{-1}	Storey et al. (2020); Okuneye et al. (2021)
K_B	Half-saturation of FGFR inhibitor	3.00×10^5	nmol L^{-1}	Estimation
d_A	Consumption rate of anti-PD-1	0.35	day^{-1}	Estimation
d_B	Consumption rate of FGFR inhibitor	0.75	day^{-1}	Estimation
K_1	Equilibrium constant of the ligand binding process	5.00×10^8	cells	Estimation
K_2	Equilibrium constant of non-ligand-dependent processes	5.00×10^3	–	Estimation
K_3	Equilibrium constant of receptor and drug binding process	1.20×10^{-3}	$L \text{ nmol}^{-1}$	Estimation

Table 5 Description of related parameters of cytokine equation

Notation	Description	Value used	Units	References
$\delta_{I_{12}D}$	Production rate of IL-12 by DCs	9.00×10^{-7}	$\text{ng mL}^{-1} \text{ day}^{-1} \text{ cell}^{-1}$	Estimation
$\delta_{I_{12}M_1}$	Production rate of IL-12 by M1	9.00×10^{-7}	$\text{ng mL}^{-1} \text{ day}^{-1} \text{ cell}^{-1}$	Estimation
$\delta_{I_2T_1}$	Production rate of IL-2 by CD4 ⁺ T cells	5.00×10^{-7}	$\text{ng mL}^{-1} \text{ day}^{-1} \text{ cell}^{-1}$	Estimation
$\delta_{I_\gamma T_1}$	Production rate of IFN- γ by CD4 ⁺ T cells	6.50×10^{-8}	$\text{ng mL}^{-1} \text{ day}^{-1} \text{ cell}^{-1}$	Estimation
$\delta_{I_\gamma T_8}$	Production rate of IFN- γ by CD8 ⁺ T cells	2.50×10^{-7}	$\text{ng mL}^{-1} \text{ day}^{-1} \text{ cell}^{-1}$	Estimation
$\delta_{T_\alpha T_1}$	Production rate of TNF- α by CD4 ⁺ T cells	8.50×10^{-9}	$\text{ng mL}^{-1} \text{ day}^{-1} \text{ cell}^{-1}$	Estimation
$\delta_{T_\alpha T_8}$	Production rate of TNF- α by CD8 ⁺ T cells	5.50×10^{-8}	$\text{ng mL}^{-1} \text{ day}^{-1} \text{ cell}^{-1}$	Estimation
$\delta_{T_\alpha M_1}$	Production rate of TNF- α by M1	8.50×10^{-8}	$\text{ng mL}^{-1} \text{ day}^{-1} \text{ cell}^{-1}$	Estimation
$\delta_{T_\beta C}$	Production rate of TGF- β by tumor cells	1.10×10^{-7}	$\text{ng mL}^{-1} \text{ day}^{-1} \text{ cell}^{-1}$	Robertson-Tessi et al. (2012)
$\delta_{T_\beta T_r}$	Production rate of TGF- β by Tregs	1.80×10^{-8}	$\text{ng mL}^{-1} \text{ day}^{-1} \text{ cell}^{-1}$	Robertson-Tessi et al. (2012)
$\delta_{T_\beta M_2}$	Production rate of TGF- β by M2	5.50×10^{-7}	$\text{ng mL}^{-1} \text{ day}^{-1} \text{ cell}^{-1}$	Estimation
$\delta_{M_C C}$	Production rate of M-CSF by tumor cells	1.20×10^{-7}	$\text{ng mL}^{-1} \text{ day}^{-1} \text{ cell}^{-1}$	Estimation
$\delta_{I_{10}C}$	Production rate of IL-10 by tumor cells	1.30×10^{-10}	$\text{ng mL}^{-1} \text{ day}^{-1} \text{ cell}^{-1}$	Robertson-Tessi et al. (2012)
$\delta_{I_{10}T_r}$	Production rate of IL-10 by tumor cells	1.40×10^{-8}	$\text{ng mL}^{-1} \text{ day}^{-1} \text{ cell}^{-1}$	Robertson-Tessi et al. (2012)
$\delta_{I_{10}M_2}$	Production rate of IL-10 by M2	1.00×10^{-10}	$\text{ng mL}^{-1} \text{ day}^{-1} \text{ cell}^{-1}$	Estimation
$d_{I_{12}}$	Degradation rate of IL-12	3.30	day^{-1}	Lui et al. (2002)
$d_{I_{10}}$	Degradation rate of IL-10	5.94	day^{-1}	Mueller et al. (2009), Saxena et al. (2015)
d_{I_2}	Degradation rate of IL-2	2.38	day^{-1}	Friedman and Hao (2018)

Table 5 continued

Notation	Description	Value used	Units	References
$d_{I\gamma}$	Degradation rate of IFN- γ	34.70	day $^{-1}$	Foon et al. (1985)
$d_{T\alpha}$	Degradation rate of TNF- α	55.00	day $^{-1}$	Oliver et al. (1993)
$d_{T\beta}$	Degradation rate of TGF- β	198.00	day $^{-1}$	Johnson et al. (2016)
d_{M_c}	Degradation rate of M-CSF	4.80	day $^{-1}$	Lai et al. (2018)

- Alexandrov LB, Nik-Zainal S, Wedge DC et al (2013) Signatures of mutational processes in human cancer. *Nature* 500(7463):415–421. <https://doi.org/10.1038/nature12477>
- Apolo AB, Infante JR, Balmanoukian A et al (2017) Avelumab, an anti-programmed death-ligand 1 antibody, in patients with refractory metastatic urothelial carcinoma: results from a multicenter, phase Ib study. *J Clin Oncol* 35(19):2117–2124. <https://doi.org/10.1200/JCO.2016.71.6795>
- Arulraj T, Wang H, Ippolito A et al (2024) Leveraging multi-omics data to empower quantitative systems pharmacology in immuno-oncology. *Brief Bioinform*. <https://doi.org/10.1093/bib/bbae131>
- Babina IS, Turner NC (2017) Advances and challenges in targeting FGFR signalling in cancer. *Nat Rev Cancer* 17(5):318–332. <https://doi.org/10.1038/nrc.2017.8>
- Balkwill F (2009) Tumour necrosis factor and cancer. *Nat Rev Cancer* 9(5):361–371. <https://doi.org/10.1038/nrc2628>
- Batlle E, Massagué J (2019) Transforming growth factor- β signaling in immunity and cancer. *Immunity* 50(4):924–940. <https://doi.org/10.1016/j.immuni.2019.03.024>
- Benjamin DJ, Hsu R (2023) Treatment approaches for FGFR-altered urothelial carcinoma: targeted therapies and immunotherapy. *Front Immunol* 14:1258388. <https://doi.org/10.3389/fimmu.2023.1258388>
- Bergholz JS, Wang Q, Kabraji S et al (2020) Integrating immunotherapy and targeted therapy in cancer treatment: mechanistic insights and clinical implications. *Clin Cancer Res* 26(21):5557–5566. <https://doi.org/10.1158/1078-0432.CCR-19-2300>
- Biot C, Rentsch CA, Gsporer JR et al (2012) Preexisting BCG-specific T cells improve intravesical immunotherapy for bladder cancer. *Sci Transl Med* 4(137):137ra72. <https://doi.org/10.1126/scitranslmed.3003586>
- Breban R, Bisiaux A, Biot C et al (2012) Mathematical model of tumor immunotherapy for bladder carcinoma identifies the limitations of the innate immune response. *OncoImmunology* 1(1):9–17. <https://doi.org/10.4161/onci.1.1.17884>
- Burgos-Simón C, García-Medina N, Martínez-Rodríguez D et al (2019) Mathematical modeling of the dynamics of the bladder cancer and the immune response applied to a patient: evolution and short-term prediction. *Math Methods Appl Sci* 42:5746–5757
- Cancer Genome Atlas Research N (2014) Comprehensive molecular characterization of urothelial bladder carcinoma. *Nature* 507(7492):315–322. <https://doi.org/10.1038/nature12965>
- Cappuccio A, Tieri P, Castiglione F (2016) Multiscale modelling in immunology: a review. *Brief Bioinform* 17(3):408–418. <https://doi.org/10.1093/bib/bbv012>
- Chen Y, Lai X (2022) Modeling the effect of gut microbiome on therapeutic efficacy of immune checkpoint inhibitors against cancer. *Math Biosci* 350:108868. <https://doi.org/10.1016/j.mbs.2022.108868>
- Chen DS, Mellman I (2013) Oncology meets immunology: the cancer-immunity cycle. *Immunity* 39(1):1–10. <https://doi.org/10.1016/j.immuni.2013.07.012>
- Chen W, Jin W, Hardegen N et al (2003) Conversion of peripheral CD4 $^{+}$ CD25 $^{-}$ Naive T cells to CD4 $^{+}$ CD25 $^{+}$ regulatory T cells by TGF- β induction of transcription factor Foxp3. *J Exp Med* 198(12):1875–1886. <https://doi.org/10.1084/jem.20030152>
- Colli LM, Machiela MJ, Zhang H et al (2017) Landscape of combination immunotherapy and targeted therapy to improve cancer management. *Cancer Res* 77(13):3666–3671. <https://doi.org/10.1158/0008-5472.CAN-16-3338>
- Dagogo-Jack I, Shaw AT (2018) Tumour heterogeneity and resistance to cancer therapies. *Nat Rev Clin Oncol* 15(2):81–94. <https://doi.org/10.1038/nrclinonc.2017.166>
- Davar D, Kirkwood JM (2019) PD-1 immune checkpoint inhibitors and immune-related adverse events: understanding the upside of the downside of checkpoint blockade. *JAMA Oncol* 5(7):942–943. <https://doi.org/10.1001/jamaoncol.2019.0413>
- de Pillis LG, Radunskaya AE, Wiseman CL (2005) A validated mathematical model of cell-mediated immune response to tumor growth. *Cancer Res* 65(17):7950–7958. <https://doi.org/10.1158/0008-5472.CAN-05-0564>
- Decker T, Müller M, Stockinger S (2005) The yin and yang of type I interferon activity in bacterial infection. *Nat Rev Immunol* 5(9):675–687. <https://doi.org/10.1038/nri1684>
- Dong C (2021) Cytokine regulation and function in T cells. *Annu Rev Immunol* 39:51–76. <https://doi.org/10.1146/annurev-immunol-061020-053702>
- Emens LA, Ascierto PA, Darcy PK et al (2017) Cancer immunotherapy: opportunities and challenges in the rapidly evolving clinical landscape. *Eur J Cancer* 81:116–129. <https://doi.org/10.1016/j.ejca.2017.01.035>

- Foon KA, Sherwin SA, Abrams PG et al (1985) A phase I trial of recombinant gamma interferon in patients with cancer. *Cancer Immunol Immunother* 20(3):193–197. <https://doi.org/10.1007/BF00205575>
- Friedlaender A, Subbiah V, Russo A et al (2022) EGFR and HER2 exon 20 insertions in solid tumours: from biology to treatment. *Nat Rev Clin Oncol* 19(1):51–69. <https://doi.org/10.1038/s41571-021-00558-1>
- Friedman A, Hao W (2018) The role of exosomes in pancreatic cancer microenvironment. *Bull Math Biol* 80(5):1111–1133. <https://doi.org/10.1007/s11538-017-0254-9>
- Gardner A, Ruffell B (2016) Dendritic cells and cancer immunity. *Trends Immunol* 37(12):855–865. <https://doi.org/10.1016/j.it.2016.09.006>
- Goel HL, Mercurio AM (2013) VEGF targets the tumour cell. *Nat Rev Cancer* 13(12):871–882. <https://doi.org/10.1038/nrc3627>
- Hamid O, Robert C, Daud A et al (2013) Safety and tumor responses with lambrolizumab (anti-PD-1) in melanoma. *N Engl J Med* 369(2):134–144. <https://doi.org/10.1056/NEJMoa1305133>
- Hughes PE, Caenepel S, Wu LC (2016) Targeted therapy and checkpoint immunotherapy combinations for the treatment of cancer. *Trends Immunol* 37(7):462–476. <https://doi.org/10.1016/j.it.2016.04.010>
- Jensen PE (2007) Recent advances in antigen processing and presentation. *Nat Immunol* 8(10):1041–1048. <https://doi.org/10.1038/ni1516>
- Jing W, Wang G, Cui Z et al (2022) FGFR3 destabilizes PD-L1 via NEDD4 to control T-cell-mediated bladder cancer immune surveillance. *Cancer Res* 82(1):114–129. <https://doi.org/10.1158/0008-5472.CAN-21-2362>
- Johnson KE, Makanji Y, Temple-Smith P et al (2016) Biological activity and in vivo half-life of pro-activin A in male rats. *Mol Cell Endocrinol* 422:84–92. <https://doi.org/10.1016/j.mce.2015.12.007>
- Karagiannidis I, Salataj E, Said Abu Egal E et al (2021) G-CSF in tumors: aggressiveness, tumor microenvironment and immune cell regulation. *Cytokine* 142:155479. <https://doi.org/10.1016/j.cyto.2021.155479>
- Katoh M (2019) Fibroblast growth factor receptors as treatment targets in clinical oncology. *Nat Rev Clin Oncol* 16(2):105–122. <https://doi.org/10.1038/s41571-018-0115-y>
- Keir ME, Butte MJ, Freeman GJ et al (2008) PD-1 and its ligands in tolerance and immunity. *Annu Rev Immunol* 26:677–704. <https://doi.org/10.1146/annurev.immunol.26.021607.090331>
- Khalife N, Chahine C, Kordahi M et al (2021) Urothelial carcinoma in the era of immune checkpoint inhibitors. *Immunotherapy* 13(11):953–964. <https://doi.org/10.2217/int-2021-0042>
- Khong HT, Restifo NP (2002) Natural selection of tumor variants in the generation of tumor escape phenotypes. *Nat Immunol* 3(11):999–1005. <https://doi.org/10.1038/ni1102-999>
- Kim JM, Chen DS (2016) Immune escape to PD-L1/PD-1 blockade: seven steps to success (or failure). *Ann Oncol* 27(8):1492–1504. <https://doi.org/10.1093/annonc/mdw217>
- Kirschner D, Panetta JC (1998) Modeling immunotherapy of the tumor-immune interaction. *J Math Biol* 37(3):235–252. <https://doi.org/10.1007/s002850050127>
- Kozłowska E, Suwiński R, Giglak M et al (2020) Mathematical model predicts response to chemotherapy in advanced non-resectable non-small cell lung cancer patients treated with platinum-based doublet. *PLoS Comput Biol* 16(10):e1008234. <https://doi.org/10.1371/journal.pcbi.1008234>
- Kuznetsov VA, Makalkin IA, Taylor MA et al (1994) Nonlinear dynamics of immunogenic tumors: parameter estimation and global bifurcation analysis. *Bull Math Biol* 56(2):295–321. <https://doi.org/10.1007/BF02460644>
- Lai X, Friedman A (2017) Combination therapy for melanoma with BRAF/MEK inhibitor and immune checkpoint inhibitor: a mathematical model. *BMC Syst Biol* 11(1):70. <https://doi.org/10.1186/s12918-017-0446-9>
- Lai X, Friedman A (2017) Combination therapy of cancer with cancer vaccine and immune checkpoint inhibitors: a mathematical model. *PLoS ONE* 12(5):e0178479. <https://doi.org/10.1371/journal.pone.0178479>
- Lai X, Stiff A, Duggan M et al (2018) Modeling combination therapy for breast cancer with BET and immune checkpoint inhibitors. *Proc Natl Acad Sci USA* 115(21):5534–5539. <https://doi.org/10.1073/pnas.1721559115>
- Lawrence T, Natoli G (2011) Transcriptional regulation of macrophage polarization: enabling diversity with identity. *Nat Rev Immunol* 11(11):750–761. <https://doi.org/10.1038/nri3088>
- Lazebnik T, Aaroni N, Bunimovich-Mendrazitsky S (2021) PDE based geometry model for BCG immunotherapy of bladder cancer. *Biosystems* 200:104319. <https://doi.org/10.1016/j.biosystems.2020.104319>

- Leommen MA, Schlessinger J (2010) Cell signaling by receptor tyrosine kinases. *Cell* 141(7):1117–1134. <https://doi.org/10.1016/j.cell.2010.06.011>
- Lenis AT, Lec PM, Chamie K et al (2020) Bladder cancer: a review. *JAMA* 324(19):1980–1991
- Li J, Wu J, Zhang J et al (2022) A multicompartment mathematical model based on host immunity for dissecting COVID-19 heterogeneity. *Heliyon* 8(5):e09488. <https://doi.org/10.1016/j.heliyon.2022.e09488>
- Liao KL, Watt KD (2022) Mathematical modeling for the combination treatment of IFN- γ and anti-PD-1 in cancer immunotherapy. *Math Biosci* 353:108911. <https://doi.org/10.1016/j.mbs.2022.108911>
- Lui VWY, He Y, Falo L et al (2002) Systemic administration of naked DNA encoding interleukin 12 for the treatment of human papillomavirus DNA-positive tumor. *Hum Gene Ther* 13(2):177–185. <https://doi.org/10.1089/10430340252769716>
- Ma S, Lei J, Lai X (2023) Modeling tumour heterogeneity of PD-L1 expression in tumour progression and adaptive therapy. *J Math Biol* 86(3):38. <https://doi.org/10.1007/s00285-023-01872-1>
- Maeng YH, Eun SY, Huh JS (2010) Expression of fibroblast growth factor receptor 3 in the recurrence of non-muscle-invasive urothelial carcinoma of the bladder. *Korean J Urol* 51(2):94–100. <https://doi.org/10.4111/kju.2010.51.2.94>
- Morales-Barrera R, Suárez C, de Castro AM et al (2016) Targeting fibroblast growth factor receptors and immune checkpoint inhibitors for the treatment of advanced bladder cancer: new direction and new hope. *Cancer Treat Rev* 50:208–216. <https://doi.org/10.1016/j.ctrv.2016.09.018>
- Mosser DM, Edwards JP (2008) Exploring the full spectrum of macrophage activation. *Nat Rev Immunol* 8(12):958–969. <https://doi.org/10.1038/nri2448>
- Mosser DM, Zhang X (2008) Interleukin-10: new perspectives on an old cytokine. *Immunol Rev* 226:205–218. <https://doi.org/10.1111/j.1600-065X.2008.00706.x>
- Mueller C, Braag SA, Martino AT et al (2009) The pros and cons of immunomodulatory IL-10 gene therapy with recombinant AAV in a Cfr^{−/−}-dependent allergy mouse model. *Gene Ther* 16(2):172–183. <https://doi.org/10.1038/gt.2008.156>
- Nikolopoulou E, Johnson LR, Harris D et al (2018) Tumour-immune dynamics with an immune checkpoint inhibitor. *Lett Biomath* 5(2):137–159
- Noy R, Pollard JW (2014) Tumor-associated macrophages: from mechanisms to therapy. *Immunity* 41(1):49–61. <https://doi.org/10.1016/j.immuni.2014.06.010>
- Okuneye K, Bergman D, Bloodworth JC et al (2021) A validated mathematical model of FGFR3-mediated tumor growth reveals pathways to harness the benefits of combination targeted therapy and immunotherapy in bladder cancer. *Comput Syst Oncol*. <https://doi.org/10.1002/cso2.1019>
- Oliver JC, Bland LA, Oettinger CW et al (1993) Cytokine kinetics in an in vitro whole blood model following an endotoxin challenge. *Lymphokine Cytokine Res* 12(2):115–120
- Patel VG, Oh WK, Galsky MD (2020) Treatment of muscle-invasive and advanced bladder cancer in 2020. *CA Cancer J Clin* 70(5):404–423. <https://doi.org/10.3322/caac.21631>
- Postow MA, Callahan MK, Wolchok JD (2015) Immune checkpoint blockade in cancer therapy. *J Clin Oncol* 33(17):1974–1982. <https://doi.org/10.1200/JCO.2014.59.4358>
- Powles T, Eder JP, Fine GD et al (2014) MPDL3280A (anti-PD-L1) treatment leads to clinical activity in metastatic bladder cancer. *Nature* 515(7528):558–562. <https://doi.org/10.1038/nature13904>
- Rizvi NA, Mazières J, Planchard D et al (2015) Activity and safety of nivolumab, an anti-PD-1 immune checkpoint inhibitor, for patients with advanced, refractory squamous non-small-cell lung cancer (CheckMate 063): a phase 2, single-arm trial. *Lancet Oncol* 16(3):257–265. [https://doi.org/10.1016/S1470-2045\(15\)70054-9](https://doi.org/10.1016/S1470-2045(15)70054-9)
- Robertson AG, Kim J, Al-Ahmadi H et al (2017) Comprehensive molecular characterization of muscle-invasive bladder cancer. *Cell* 171(3):540–556. <https://doi.org/10.1016/j.cell.2017.09.007>
- Robertson-Tessi M, El-Kareh A, Goriely A (2012) A mathematical model of tumor-immune interactions. *J Theor Biol* 294:56–73. <https://doi.org/10.1016/j.jtbi.2011.10.027>
- Rosenbaum MI, Clemmensen LS, Bredt DS et al (2020) Targeting receptor complexes: a new dimension in drug discovery. *Nat Rev Drug Discov* 19(12):884–901. <https://doi.org/10.1038/s41573-020-0086-4>
- Rozen SG (2020) Mutational selection in normal urothelium. *Science* 370(6512):34–35. <https://doi.org/10.1126/science.abe0955>
- Rubtsov YP, Rasmussen JP, Chi EY et al (2008) Regulatory T cell-derived interleukin-10 limits inflammation at environmental interfaces. *Immunity* 28(4):546–558. <https://doi.org/10.1016/j.immuni.2008.02.017>
- Santana-Davila R, Bhatia S, Chow LQM (2017) Harnessing the immune system as a therapeutic tool in virus-associated cancers. *JAMA Oncol* 3(1):106–112. <https://doi.org/10.1001/jamaoncol.2016.4574>

- Saxena A, Khosraviani S, Noel S et al (2015) Interleukin-10 paradox: a potent immunoregulatory cytokine that has been difficult to harness for immunotherapy. *Cytokine* 74(1):27–34. <https://doi.org/10.1016/j.cyto.2014.10.031>
- Schachter J, Ribas A, Long GV et al (2017) Pembrolizumab versus ipilimumab for advanced melanoma: final overall survival results of a multicentre, randomised, open-label phase 3 study (KEYNOTE-006). *Lancet* 390(10105):1853–1862. [https://doi.org/10.1016/S0140-6736\(17\)31601-X](https://doi.org/10.1016/S0140-6736(17)31601-X)
- Schneider AK, Chevalier MF, Derré L (2019) The multifaceted immune regulation of bladder cancer. *Nat Rev Urol* 16(10):613–630. <https://doi.org/10.1038/s41585-019-0226-y>
- Shaikh L, Bumimovich-Mendrazitsky S (2018) Stability analysis of delayed immune response BCG infection in bladder cancer treatment model by stochastic perturbations. *Comput Math Methods Med* 2018:9653873. <https://doi.org/10.1155/2018/9653873>
- Sharma P, Allison JP (2015) Immune checkpoint targeting in cancer therapy: toward combination strategies with curative potential. *Cell* 161(2):205–214. <https://doi.org/10.1016/j.cell.2015.03.030>
- Siewe N, Friedman A (2021) TGF-beta inhibition can overcome cancer primary resistance to PD-1 blockade: a mathematical model. *PLoS ONE* 16(6):e0252620. <https://doi.org/10.1371/journal.pone.0252620>
- Singh AK, Praharaj M, Lombardo KA et al (2022) Re-engineered BCG overexpressing cyclic di-AMP augments trained immunity and exhibits improved efficacy against bladder cancer. *Nat Commun* 13(1):878. <https://doi.org/10.1038/s41467-022-28509-z>
- Smith LK, Boukhaled GM, Condotta SA et al (2018) Interleukin-10 directly inhibits CD8⁺ T cell function by enhancing N-glycan branching to decrease antigen sensitivity. *Immunity* 48(2):299–312. <https://doi.org/10.1016/j.immuni.2018.01.006>
- Soto-Ortiz L, Finley SD (2016) A cancer treatment based on synergy between anti-angiogenic and immune cell therapies. *J Theor Biol* 394:197–211. <https://doi.org/10.1016/j.jtbi.2016.01.026>
- Spolski R, Li P, Leonard WJ (2018) Biology and regulation of IL-2: from molecular mechanisms to human therapy. *Nat Rev Immunol* 18(10):648–659. <https://doi.org/10.1038/s41577-018-0046-y>
- Storey KM, Lawler SE, Jackson TL (2020) Modeling oncolytic viral therapy, immune checkpoint inhibition, and the complex dynamics of innate and adaptive immunity in glioblastoma treatment. *Front Physiol* 11:151. <https://doi.org/10.3389/fphys.2020.00151>
- Tanaka A, Sakaguchi S (2017) Regulatory T cells in cancer immunotherapy. *Cell Res* 27(1):109–118. <https://doi.org/10.1038/cr.2016.151>
- Tomlinson DC, Baldo O, Harnden P et al (2007) FGFR3 protein expression and its relationship to mutation status and prognostic variables in bladder cancer. *J Pathol* 213(1):91–98. <https://doi.org/10.1002/path.2207>
- Topalian SL, Hodi FS, Brahmer JR et al (2012) Safety, activity, and immune correlates of anti-PD-1 antibody in cancer. *N Engl J Med* 366(26):2443–2454. <https://doi.org/10.1056/NEJMoa1200690>
- Tran L, Xiao JF, Agarwal N et al (2021) Advances in bladder cancer biology and therapy. *Nat Rev Cancer* 21(2):104–121. <https://doi.org/10.1038/s41568-020-00313-1>
- Trinchieri G (2003) Interleukin-12 and the regulation of innate resistance and adaptive immunity. *Nat Rev Immunol* 3(2):133–146. <https://doi.org/10.1038/nri1001>
- Tripathi SK, Lahesmaa R (2014) Transcriptional and epigenetic regulation of T-helper lineage specification. *Immunol Rev* 261(1):62–83. <https://doi.org/10.1111/imr.12204>
- Tscharke DC, Croft NP, Doherty PC et al (2015) Sizing up the key determinants of the CD8(+) T cell response. *Nat Rev Immunol* 15(11):705–716. <https://doi.org/10.1038/nri3905>
- Tumeh PC, Harview CL, Yearley JH et al (2014) PD-1 blockade induces responses by inhibiting adaptive immune resistance. *Nature* 515(7528):568–571. <https://doi.org/10.1038/nature13954>
- Ulloa L, Doody J, Massagué J (1999) Inhibition of transforming growth factor- β /SMAD signalling by the interferon- γ /STAT pathway. *Nature* 397(6721):710–713. <https://doi.org/10.1038/17826>
- van Kessel KEM, Zuiverloon TCM, Alberts AR et al (2015) Targeted therapies in bladder cancer: an overview of in vivo research. *Nat Rev Urol* 12(12):681–694. <https://doi.org/10.1038/nrurol.2015.231>
- Walshaw RC, Honeychurch J, Illidge TM et al (2018) The anti-PD-1 era—an opportunity to enhance radiotherapy for patients with bladder cancer. *Nat Rev Urol* 15(4):251–259. <https://doi.org/10.1038/nrurol.2017.172>
- Wang H, Arulraj T, Kimko H et al (2023) Generating immunogenomic data-guided virtual patients using a QSP model to predict response of advanced NSCLC to PD-L1 inhibition. *NPJ Precis Oncol* 7(1):55. <https://doi.org/10.1038/s41698-023-00405-9>

- Ward Grados DF, Ahmadi H, Griffith TS et al (2022) Immunotherapy for bladder cancer: latest advances and ongoing clinical trials. *Immunol Invest* 51(8):2226–2251. <https://doi.org/10.1080/08820139.2022.2118606>
- Wculek SK, Cueto FJ, Mujal AM et al (2020) Dendritic cells in cancer immunology and immunotherapy. *Nat Rev Immunol* 20(1):7–24. <https://doi.org/10.1038/s41577-019-0210-z>
- Wołacewicz M, Hrynkiewicz R, Grywalska E et al (2020) Immunotherapy in bladder cancer: current methods and future perspectives. *Cancers (Basel)* 12(5):1181
- Xue L, Zhang H, Zheng X et al (2023) Treatment of melanoma with dendritic cell vaccines and immune checkpoint inhibitors: a mathematical modeling study. *J Theor Biol* 568:111489. <https://doi.org/10.1016/j.jtbi.2023.111489>
- Yamaguchi H, Hsu JM, Yang WH et al (2022) Mechanisms regulating PD-L1 expression in cancers and associated opportunities for novel small-molecule therapeutics. *Nat Rev Clin Oncol* 19(5):287–305. <https://doi.org/10.1038/s41571-022-00601-9>
- Yu JL, Jang SRJ (2019) A mathematical model of tumor-immune interactions with an immune checkpoint inhibitor. *Appl Math Comput* 362:124523
- Zhou L, Chong MMW, Littman DR (2009) Plasticity of CD4⁺ T cell lineage differentiation. *Immunity* 30(5):646–655. <https://doi.org/10.1016/j.immuni.2009.05.001>
- Zhu J, Paul WE (2008) CD4 T cells: fates, functions, and faults. *Blood* 112(5):1557–1569. <https://doi.org/10.1182/blood-2008-05-078154>

Publisher's Note Springer Nature remains neutral with regard to jurisdictional claims in published maps and institutional affiliations.

Springer Nature or its licensor (e.g. a society or other partner) holds exclusive rights to this article under a publishing agreement with the author(s) or other rightsholder(s); author self-archiving of the accepted manuscript version of this article is solely governed by the terms of such publishing agreement and applicable law.